Powder Technology 329 (2018) 181–198

Contents lists available at ScienceDirect

Powder Technology

journal homepage: www.elsevier.com/locate/powtec

A transient model for nozzle clogging

H. Barati [a,b], M. Wu [a,*], A. Kharicha [a], A. Ludwig [a]

[a] Chair for Modeling and Simulation of Metallurgical Processes, Department of Metallurgy, Montanuniversitaet, Franz-Josef Street 18, 8700 Leoben, Austria
[b] K1-MET, Franz-Josef Street 18, 8700 Leoben, Austria

ARTICLE INFO

Article history:
Received 6 December 2017
Received in revised form 16 January 2018
Accepted 20 January 2018
Available online 02 February 2018

Keywords:
Clogging
Fouling
Eulerian-Lagrangian
Particle
Continuous casting

ABSTRACT

This model has been developed for transient simulation of clogging (also called as fouling) in submerged entry nozzle (SEN) during continuous casting. Three major steps of the clogging have been taken into account: (a) transport of non-metallic inclusions (NMIs) by turbulent melt flow towards the SEN wall; (b) interactions between melt and wall, and the adhesion of the NMI on the wall; (c) formation and growth of the clog by NMI deposition. The computational domain is divided into bulk and near-wall regions. An Eulerian-Lagrangian approach is employed to calculate the transport of NMIs by the turbulent flow; a stochastic near-wall model is adopted to trace particles in the turbulent boundary layer (near-wall region). The early stage of clogging is modeled by the dynamical change in wall roughness, while the late stage of the clogging is modeled by building a layer of porous clog region from the wall. This layer is called as 'clog', and it continues to grow by attaching more NMI particles. To evaluate the model, a laboratory experiment, which was designed to study the clogging of SEN during steel continuous casting, is simulated. It is verified that the model can reproduce the experiment: the calculated clogged section of the nozzle is qualitatively comparable with as-clogged sections in laboratory experiments; the calculated mass flow rate through the nozzle agrees with the experimentally-monitored result as well. New knowledge is obtained. (1) Clogging is a transient process interacting with the melt flow, and it includes the initial coverage of the nozzle wall with deposited particles, the evolution of a bulged clog front, and then the development of a branched structure. (2) Clogging is a stochastic and self-accelerating process. Finally, model capabilities/limitations, uncertainties for choosing the modeling parameters such as mesh size, Lagrangian time scale, the correction factor in the interpolation of clog permeability are studied and discussed.

1. Introduction

Blockage of the fluid route due to the deposition and accumulation of solid suspended particles on the fluid passage wall is a common problem in a vast area of scientific fields and engineering applications such as heat exchangers [1], exhaust gas recirculation coolers in the automotive industry [2], food productions like wine microfiltration [3], membrane fouling in pharmaceutical industries [4], and nozzle clogging in steel continuous casting [5]. This phenomenon is usually termed as clogging or fouling. The Occurrence of clogging is a complex process. As depicted in Fig. 1, it mainly comprises four steps: (a) the turbulent fluid flow and the transport of the suspended particles towards the wall; (b) the interaction of the fluid with the wall and adhesion mechanism of the particles on the wall; (c) formation and growth of the clog; (d) fragmentation of the clog by the fluid flow to form fragments. In some cases, chemical reactions, electrostatic interactions at the fluid-wall interface, or even freezing (solidification) of the fluid on the wall might occur. Extensive research and great effort have been undertaken in order to gain a better understanding of clogging mechanisms in recent years.

Steps (a) and (b) of Fig. 1 are supposed to be major mechanisms for clogging/fouling, i.e. the hydrodynamic transport of particles and the adhesion mechanism [6]. For example, a study on fouling in a heat exchanger (water flow with silica suspensions of ~1 μm) shows that hydrodynamic lift forces gain complete control of the deposition process, and thermophoresis enhances deposition onto cooled surfaces [7]. A study on the transport and deposition of hematite particles on glass shows the importance of ionic charge strength [8]: at very low ionic strength, only monolayer deposition was observed, while at high ionic strength multilayer deposition became significant. This mechanism was further verified by another investigation on a polymeric microfluidic filtration device where fouling of the micro-channels by micron-sized (4.9 μm) particles occurred [9]. Particles at low ionic strength (more hydrophilic conditions) did not lead to the blockage of the micro-channels by fouling, while particles at high ionic strength (more hydrophobic conditions) led to rapid and complete fouling of the micro-channels.

During continuous casting of steel, the liquid melt is fed through a submerged entry nozzle (SEN) into the casting mold. SEN clogging is a long-term problem, leading to operation disruptions and different

* Corresponding author.
E-mail address: menghuai.wu@unileoben.ac.at (M. Wu).

https://doi.org/10.1016/j.powtec.2018.01.053
0032-5910/

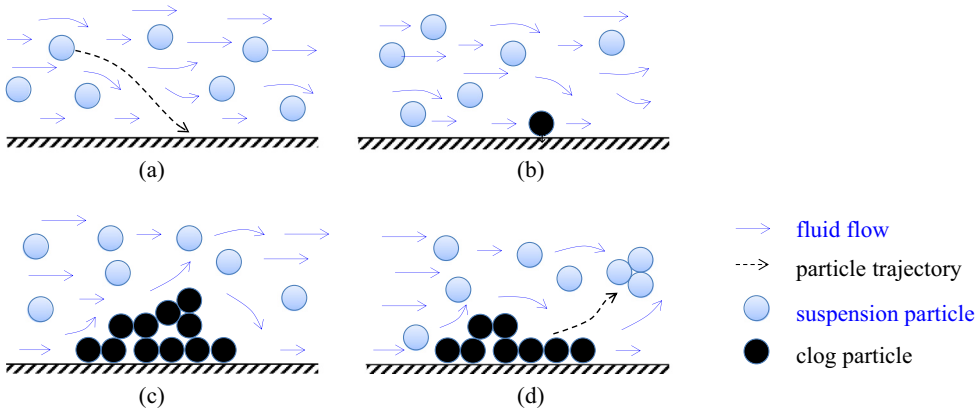

Fig. 1. Schematic of clogging/fouling phenomenon (four steps).

casting defects [10–12]. Great attention has been paid to the issue of SEN clogging during continuous casting of steel, as it may result in asymmetrical melt flow in the mold and therefore affect the solidification pattern [10], introduce macro-inclusion through the detachment/resuspension of the clog periodically [13], even terminate the process in the worst case [12]. High process temperatures, potential chemical reactions, possible phase change of the melt (solidification), and the electro-conductive nature of molten steel might result in the occurrence of different clogging mechanisms in comparison with those as studied in other fields. Various mechanisms for SEN clogging are suggested: (1) attachment of de-oxidation and re-oxidation products on the SEN wall [14–16]; (2) thermochemical reactions in the melt at the SEN wall leading to in-situ formation of oxide products [11,17]; (3) negative pressure drawing oxygen through the SEN refractory pores into the inner SEN wall and reaction of oxygen with the steel melt to form oxides [18]; (4) temperature drop of the melt leading to lower solubility of oxygen in the steel melt and resulting in precipitation of alumina at SEN-steel interface [19,20]; and (5) possible solidification of the steel melt on the SEN wall [21,22]. Although various diverse opinions on the SEN clogging mechanisms exist, evidence shows that the deposition of non-metallic inclusions (NMIs) of de-oxidation and re-oxidation products on the SEN wall is still the primary cause of clogging [5]. The inclusions mainly consist of Al_2O_3 in aluminum killed steel. Depending on the steel grade, other NMIs such as TiN, TiO_2, ZrO_2, CaS, and rare earth oxides have been observed [23,24]. They originate from the steel melt [16,25], and their typical size is 2–10 μm [26]. They also have different shapes and can occur as either globular, clusters, dendrites, coral-shaped clusters, faceted particles, and even irregular plates [26–30]. However, globular shaped NMIs most frequently appear. Similar morphologies and chemical compositions of NMIs can be observed in the melt, in the clog material, and in the as-cast product [31]. Moreover, investigations for nozzle materials did not find a statistical difference in the mean rate of clogging for alumina, zirconia, magnesia, and zirconia-graphite nozzles [32].

Different numerical models have been developed to simulate the clogging/fouling phenomenon by emphasizing one or more critical steps evident in Fig. 1. The simplest method is the single-phase-based Eulerian approach. The bulk flow is solved, while the motion of the particles is not tracked explicitly. For example, by changing the geometry manually to mimic the build-up of alumina clog on the inner wall of the nozzle, Bai and Thomas studied the effect of the clog on the flow through a slide-gate nozzle [33]. The simulation results showed that the initial clogging around the slide gate enhances the melt flow rate initially due to a streamlining effect. After severe clogging, the flow is eventually restricted, so the gate opening has to be enlarged to ensure a constant casting speed. Zhang and co-workers used a similar method, e.g. by blocking half of one out-port of the SEN manually, to study the clog-induced asymmetrical flow in the mold, the locally-superheated region and the increased risk of breakouts [10].

The most frequently-used numerical method is the Eulerian-Lagrangian approach, with which both fluid flow and particle motion are calculated. The particles are defined as a discrete phase, for which the motion trajectories are calculated in a Lagrangian frame of reference, while the fluid flow is calculated with Eulerian approach [28,34,35]. This type of model was used to correlate the flow pattern, as caused by different SEN designs, with the clogging tendency [23]. It could also be used to study the influence of the velocity gradient of the melt flow, the turbulent kinetic energy, and the irregularity of flow pattern on the particle deposition tendency [36]. Most studies based on this method focus only on the fluid flow and particle transport, i.e. step (a) of Fig. 1. Although some fluid-wall interactions (e.g. the wall roughness of the SEN and its influence on the flow) could be taken into account [24], the adhesion mechanism (step (b)) and the growth of the clog (step (c)) are ignored.

The Eulerian-Eulerian two-phase approach is also used to study the clogging phenomenon. Here the particles are treated as a secondary Eulerian phase. For example, Ni et al. used this approach to predict the inclusion deposition rate in a SEN where Brownian and turbulent diffusion, turbophoresis, and thermophoresis were considered as transport mechanisms [37,38]. Effects of different process parameters and materials properties on clogging were also studied. A similar Eulerian-Eulerian model was developed by Eskin et al. to explain particle deposition in a vertical, turbulent pipe flow [39]. Again, the adhesion mechanism of the particles on the nozzle wall (step (b)) cannot be considered and the growth of the clog (step (c)) is to be ignored.

The most promising model, which can really cover clogging steps ((a)–(c) in Fig. 1), was recently proposed by Caruyer et al. [40]. They simulated multilayer deposition of particles with a diameter of 80 μm on the bore surface of a pipe, by using an Eulerian-Lagrangian method. The researchers studied fluid velocity modification by deposition over time. In their simulation, the deposited material is supposed to be a closely packed, porous medium, formed by identically sized spherical particles. In addition, their findings lead to the conclusion that incoming particles will always deposit on the wall or other adhering particles.

The current paper presents a new model for simulating the transient clogging process in SEN during continuous casting of steel, covering steps (a)–(c). An Eulerian-Lagrangian approach is applied for the transport of suspended particles along with a special focus on fluid structure near the wall, similar to the method employed by [40] (step (a)). A simplified treatment is implemented to the model for the interaction between particles and the rough wall (step (b)) and a new algorithm is taken to track the growth of the clog (step (c)). This algorithm was originally developed for tracking the solidification front of the columnar dendrite structure [41,42], but here it has been modified to track the

front of the clog. Additionally, the initial stage of clogging is subject to special treatment. The surface roughness of the SEN, its influences on the flow and on the initial build-up of the clog are taken into account. The model has general features of clogging/fouling and should be applicable to broad fields, however, the focus of this paper is on the clogging phenomenon in submerged entry nozzle (SEN) during continuous casting of steel.

The model is evaluated against a laboratory experiment [29]. Steel is melted and deoxidized in an induction furnace, then teemed through a small nozzle into a container. The nozzle may be clogged by de-oxidation by-products, and clogging rates can be estimated by weighing the mass of the melt – as collected in the container. Metallographic images of the as-cast nozzle section can be obtained as additional information to evaluate the model.

2. Numerical model

2.1. General description/model assumptions

As shown in Fig. 1, we consider the clogging process in four steps. Correspondingly, the model should be divided into four parts. In the current version of the model, however, step (d) is neglected. General model assumptions for each step are listed below.

(a) Transport of the suspended particles by turbulent flow

- An Eulerian model is employed to calculate the turbulent flow.
- Steel melt behaves as an incompressible Newtonian fluid.
- To model turbulent flow, the shear-stress transport (SST) k-ω model is applied.
- Steel melt is assumedly isothermal; therefore, heat transfer and solidification do not occur.
- A Lagrangian model tracks the motion of the particles since the volume fraction of particles in the bulk melt is much smaller than 0.1.
- Non-metallic inclusions are rendered as spherical particles which are chemically inert.
- Interactions between particles are neglected because of low concentrations of inclusions in the steel melt. Hence, there is no coagulation.
- Constant material properties of the steel melt and particles are applied.
- In the bulk melt, the one-way coupling between particle motion and fluid flow is applied: flow influences particle motion, but particle motion does not influence the flow.

(b) Interaction of the fluid with the wall and adhesion mechanism of the particles

- The laminar sub-layer adjacent to the wall is neglected due to the wall's roughness.
- Particles mechanically stick when they reach the wall.
- No chemical reaction occurs on the wall.
- Van der Waals force between the wall and the particle is not taken into account due to the adhesion mechanism of NMI on refractory wall explained in §2.3.
- Particles carry no electrostatic charge because molten steel is electrically conductive.
- Equivalent sand-grain roughness is used for the wall changing dynamically by particle deposition.

(c) Formation and growth of the clog

- The mechanism of deposition on the clog is the same as that of particle deposition on the wall.
- The clog is a porous medium with open pores.
- Clog porosity information is extracted from a postmortem analysis of experimental clog samples.
- A volume-average scheme is used to define clog properties, e.g. porosity, in computational cells.

2.2. Flow and particle transport

The melt flow as the primary continuous medium is described by the conservation equations of mass and momentum. To model the turbulent flow, shear-stress transport (SST) k-ω model is adopted. It effectively blends the robust and accurate formulation of the k-ω model in the near-wall region with the free-stream independence of the k-ε model in the far field [43]. The equation set for the turbulent flow is in Table 1. In these equations, $\vec{S}_u$, S_k, and S_ω are source terms in porous clog material for velocity, k, and ω, respectively, which are expressed by Eqs. (19)–(21).

Direct Numerical Simulation (DNS) has shown that the flow in the turbulent boundary layer consists of quasi-stream-wise coherent vortices, called “coherent structure”. Transport of particles towards or from the wall is controlled by these structures, and there is a strong correlation between the coherent structures near the wall and the particle deposition on the wall [44]. Therefore, two different particle tracking models have been adopted in the present model: one for the particle transport in the bulk fluid and one for the particle transport near the wall.

2.2.1. Particle transport in bulk fluid

The motion of particles in the bulk melt is calculated by solving the standard equations in a Lagrangian frame of reference. The solid non-metallic inclusions are assumed as a discrete secondary phase with a spherical shape. It is, in fact, a force balance of the buoyancy ($\vec{F}_B$), drag ($\vec{F}_D$), lift ($\vec{F}_L$), virtual mass ($\vec{F}_{VM}$), and pressure gradient ($\vec{F}_{press}$), respectively.

$$m_p \frac{d\vec{u}_p}{dt} = \vec{F}_B + \vec{F}_D + \vec{F}_L + \vec{F}_{VM} + \vec{F}_{press} \tag{5}$$

The equations for these forces are listed in Table 2. Additionally, a random walk model is an auxiliary for treating the chaotic motion of particles due to the turbulence. Thus, the instantaneous fluid velocity, $\vec{u'}$, as calculated by the following equation, is implemented in drag force term:

$$\vec{u'} = \vec{u} + \xi\sqrt{\frac{2k}{3}}. \tag{11}$$

$\vec{u}$ is the time averaged velocity as calculated by the governing equations (Table 1) and ξ is a Gaussian distributed random number. The second term on the right hand side denotes turbulent fluctuation.

2.2.2. Particle transport in near-wall region

In turbulent boundary layers, particles moving towards and from the wall are mainly governed by interactions between particles and so-

Table 1
Governing equations for the fluid flow.

Conservation equations		
Mass	$\nabla\cdot(\rho\vec{u}) = 0$	(1)
Momentum	$\rho\frac{\partial\vec{u}}{\partial t} + \nabla\cdot(\rho\vec{u}\vec{u}) = -\nabla p + \nabla\cdot(\mu\nabla\vec{u}) + \vec{S}_u$	(2)
Turbulence kinetic energy	$\rho\frac{\partial k}{\partial t} + \nabla\cdot(\rho k\vec{u}) = \nabla\cdot(\Gamma_k\nabla k) + \tilde{G}_k - Y_k + S_k$	(3)
Specific dissipation rate	$\rho\frac{\partial\omega}{\partial t} + \nabla\cdot(\rho\omega\vec{u}) = \nabla\cdot(\Gamma_\omega\nabla k) + G_\omega - Y_\omega + D_\omega + S_\omega$	(4)

Table 2
Equations for forces acting on a particle in bulk flow [28].

Force		
Buoyancy	$\vec{F}_B = \frac{(\rho_p-\rho)\pi d_p^3}{6}\vec{g}$	(6)
Drag	$\vec{F}_D = \frac{1}{8}\pi d_p^2 \rho C_D \lvert\vec{u}-\vec{u}_p\rvert(\vec{u}-\vec{u}_p)$	(7)
	$C_D = \begin{cases} \frac{24}{Re_p}, & Re_p<0.1 \\ \frac{24}{Re_p}(1+0.15\,Re_p^{0.687}), & 0.1\le Re_p\le 10^3 \\ 0.44, & Re_p>10^3 \end{cases}$	
	$Re_p = \frac{\lvert\vec{u}-\vec{u}_p\rvert d_p \rho}{\mu}$	
Lift	$\vec{F}_L = -\frac{9}{4\pi}\mu d_p^2 U_s\ \mathrm{sgn}(G)(\frac{\rho}{\mu}\lvert G\rvert)^{\frac{1}{2}}\vec{J}$	(8)
Virtual mass	$\vec{F}_{VM} = \frac{\rho\pi d_p^3}{12}\frac{d}{dt}(\vec{u}-\vec{u}_p)$	(9)
Pressure gradient	$\vec{F}_{press} = \frac{\rho\pi d_p^3}{6}\frac{D\vec{u}}{Dt}$	(10)

called 'coherent structures' of the flow. To solve the coherent structures and their interaction with particles explicitly, it is crucial to conduct Direct Numerical Simulation (DNS) with superfine mesh [44]. The DNS calculation is not practical for engineering applications. Therefore, here an alternative near-wall model, taken from Guingo and Minier [45], has been applied to mimic particle motion in the coherent structures by a stochastic approach. This model comprises a succession of simple sub-models instead of one complex model for the coherent structures. As shown in Fig. 2 and described in the previous section (§2.2.1), transport of the particle in the bulk ($y^+ \geq 100$, according to the law of the wall) is treated by the random walk model. When a particle enters into the turbulent boundary layer ($y^+ < 100$), the near-wall stochastic model controls the particle motion. In the present work, we neglect the laminar sublayer due to the wall roughness. Further explanation of this assumption will appear in the next section (§2.3).

In the turbulent boundary layer, due to the interactions between the coherent structures and the particle, three states of particle motion are considered [45]: (1) going towards the wall, called 'sweep'; (2) moving randomly along the wall direction as called 'diffusion', and, (3) escaping from the wall, called 'ejection'. The state of particle motion is denoted by a S index ($S\epsilon\{1,2,3\}$): 1 for sweep, 2 for diffusion, 3 for ejection. The state of motion, i.e. S index, jumps randomly between 1, 2 and 3 with time corresponding to changes from one coherent structure to another. It means that S index is a function of time, $S(t)$. Currently, there is no robust function to define the lifetime for the state of motion, τ_s. According to the dimensionless values suggested by [45], we use the following equation to find τ_s.

$$\tau_s = \begin{cases} 9T_L\ \ln(r), S(t)=1,3 \\ 3T_L\ \ln(r), S(t)=2 \end{cases} \quad (12)$$

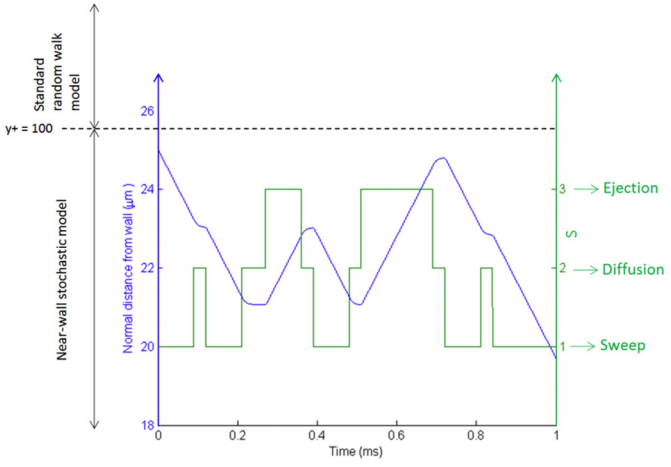

Fig. 2. An example of alumina particle trajectory in steel melt flow in a near-wall region.

T_L is the Lagrangian time scale (10^{-6}–10^{-5} s), and dependency of the modeling result on this value will be analyzed in next sections. r is a random number.

In the near-wall region, the velocity of fluid and particle is calculated in a local coordinate system where a component should be in wall normal direction. If the local coordinate system is not coincident with the global coordinate system of simulation, the results of near-wall region must be converted to the global system. The wall-normal component of the fluid velocity in the boundary layer seen by the particle is defined as 'velocity seen', u_s. A simple expression is proposed:

$$u_s = \begin{cases} -\sqrt{0.39k}, & S(t)=1 \\ u_s' - \frac{u_s}{T_L}dt + KdW(t), & S(t)=2 \\ \sqrt{0.39k}, & S(t)=3 \end{cases} \quad (13)$$

u_s, for the state of sweep and ejection is estimated according to the fluid velocity in the coherent structure $\sqrt{0.39k}$, where k is turbulence kinetic energy (personal communication with C. Henry, one of the developers of the near-wall stochastic model, 2016). The velocity seen for the state of diffusion is progressively calculated, based on the value of the last (Lagrangian) time step, u_s', by adding a noise term, KdW. The initial value of u_s' is taken as the fluid velocity. $K = 0.68\sqrt{k/T_L}$ is the diffusion coefficient and $W(t)$ is the Wiener process, whose increments $dW(t) = W(t+dt) - W(t)$ represent the effects of a noise term [46]. Here, $dW(t)$ is a Gaussian random number with mean value of 0, and variance equals particle time step.

Based on the u_s, the wall normal velocity of the particle, u_p, can be calculated as

$$\frac{du_p}{dt} = \frac{u_s - u_p}{\tau_p} + K_{Br}\frac{dW}{dt}, \quad (14)$$

τ_p is the particle relaxation time, $\sqrt{4\rho_p d_p/(3\rho C_D\lvert u_s-u_p\rvert)}$. Again, a so-called *white-noise term* is considered according to the Wiener process, where K_{Br} is velocity diffusion term [45].

$$K_{Br} = \sqrt{\frac{2k_B T}{m_p \tau_p}}, \quad (15)$$

where k_B is Boltzmann constant, m_p is the mass of the particle, and T is the fluid temperature.

There should be a thin laminar sub-layer adjacent to the wall. Here we neglect this layer because calculation results using empirical equations of y^+ show that the laminar sub-layer is very thin due to the wall roughness in this particular case.

2.3. Adhesion mechanism

Interaction between non-metallic inclusions (NMI) and the refractory wall, made of refractory material or ceramic, in molten steel is an important subject for metallurgists [47–50]. Findings show that capillary force, also termed adhesion force, is the main reason for particles adhering to the wall. Adhesion force is, in fact, due to the surface tension of the melt on a meniscus formed between the NMI particle and SEN wall. When the particle approaches the wall, a rupture of the disjoining liquid film between them occurs. Then, the fluid is drained out of the particle-wall contact because of the low wettability of alumina by steel melt and gas capillary forms [48]. A comparison of capillary force and other forces which might move the particle from the contact with the wall, like drag force and lift force, shows that capillary force is at least a few orders of magnitude larger. Therefore, one can conclude that once the capillary force is imposed, the particle remains attached to the wall [48–50]. Moreover, the sinter bond between the alumina particle and SEN wall (or attached particle) forms rapidly at high

temperatures [47]. In another case, low pressure develops in the SEN (e.g. in the gap between the stopper rod and the top of the SEN). This low pressure probably leads to degassing of the liquid steel. Accordingly, cavities on the surface of the particle and pores of the SEN wall act as nucleation sites for gas bubbles [51]. Thus, when a particle comes into contact with the SEN wall, a gas bubble may already exist between them. This may raise the tendency towards clogging in the upper part of the SEN. Therefore, considering the aforementioned aspects, it is assumed that the NMI particles stick to the SEN wall as they pass through the turbulence boundary layer and reach the wall. This means that the rate-controlling step is the transport of particles from the bulk molten steel to the wall.

The surface roughness of the SEN wall plays a crucial role in the fluid flow near the wall, hence, it influences the transport of the particles to or from the wall. To model the wall roughness effects, the law-of-the-wall for mean velocity is modified using an additive term which depends on the nature and size of troughs and hollows causing the roughness. This term has been found to be well-correlated with the dimensionless roughness height, $K_s^+ = \rho K_s u^*/\mu$, for a uniform sand-grain roughness, as shown in Fig. 3(b). K_s is the physical roughness height. u^* is a velocity function which is determined by the turbulence kinetic energy (k) with a relation, $u^* = C_\mu^{1/4} k^{1/2}$, where C_μ is a turbulence constant [43]. The wall roughness influences the turbulence kinetic energy (k) of the flow, which in turn influences particle motion in the boundary layer (§2.2.2).

Deposition of particles on the wall alters the wall roughness. In the current model, we consider the change of the wall roughness resulting from particle deposition. The initial surface roughness profile, given by experimental measurements, should be converted to an equivalent sand-grain roughness. Adams et al. suggest a simple algorithm to relate the measured surface roughness to an equivalent sand-grain roughness [52], as shown in Fig. 3.

$$K_s = 5.863\overline{R}_a, \tag{16}$$

where $\overline{R}_a$ is the arithmetic average of distances of the surface profile from the average height of the profile. An arbitrary roughness profile and the average height of asperities are plotted in Fig. 3(a). The equivalent height as sand-grain roughness in the control volume (cell) is illustrated in Fig. 3(b).

To implement the unsteady change of roughness due to the particle deposition, an increase of the deposited material is simply considered as an increase of sand grain height in each computational cell adjacent to the wall. The deposited particles are deleted from the calculation domain. As shown in Fig. 3(c), in every time step the thickness of deposited material on the wall is calculated as K_s^{new}. It is noteworthy that the deposited material, here also named as 'clog', is porous, and the average solid volume fraction of the clog ($\overline{f}_p$) can be determined experimentally. Therefore, in the calculation of the thickness of the deposition ($(K_s^{new} - K_s)/2$) the porosity of the clog must be taken into account.

If K_s^{new} grows by more than half of the cell size ($\Delta y/2$), the current computation cell adjacent to the wall surface is treated as porous medium, marked in yellow (Fig. 3(d)). We assume that the whole SEN surface, which belongs to the current computational cell, is fully covered by the deposited particles. The change of the cell's status to yellow announces the termination of step (b) and the beginning of step (c) in Fig. 1, i.e. the clog growth. Cell status is explained in the next section explicitly.

2.4. Clog growth

Metallographic analysis (SEM) of the clogged nozzle of a pilot plant setup [29,53] has shown that clog material is porous (Fig. 4). The main part of the clog is composed of non-metallic inclusions (NMIs), e.g. alumina, which forms a porous network. Furthermore, distribution of the NMIs in the clog is not homogenous. We describe the clog with following parameters: the diameter of alumina particle d_p, the average volume fraction of the clog $\overline{f}_p$, and the diameter of large pores D_{pore}. As shown in Fig. 4, some large pores with size of D_{pore} exist. All those parameters can be determined experimentally, and they are used as input parameters

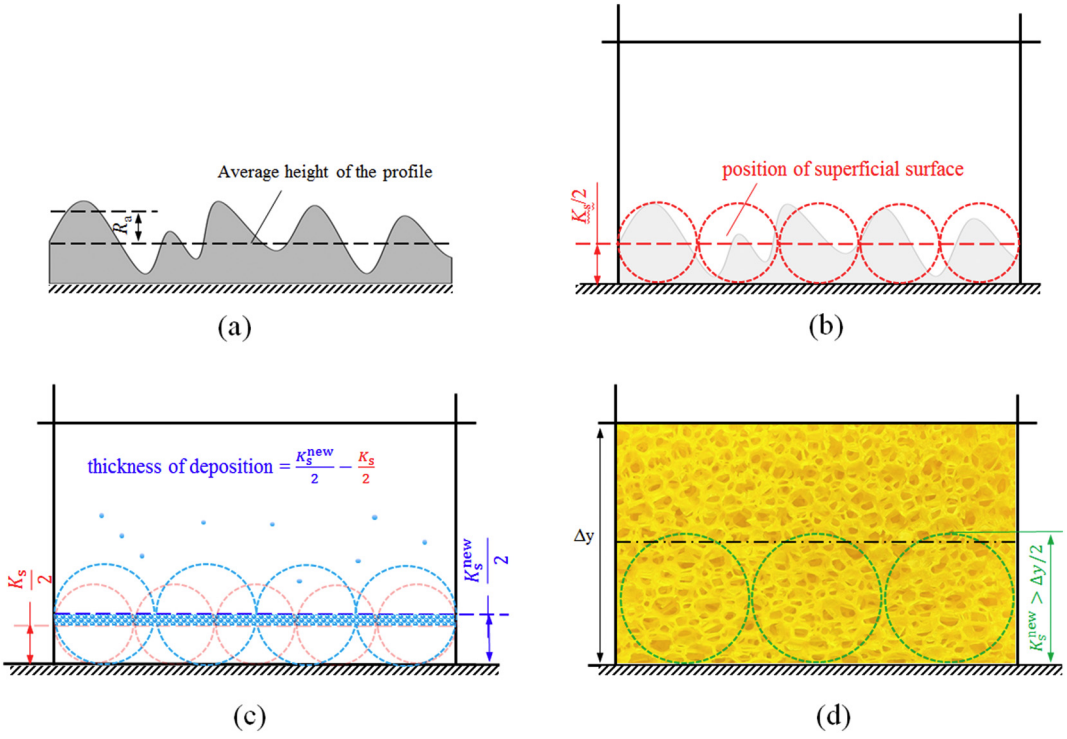

Fig. 3. Change of roughness by particle deposition: (a) an arbitrary roughness profile, (b) equivalent sand-grain roughness, (c) increase in roughness height, (d) convert cell to a porous medium.

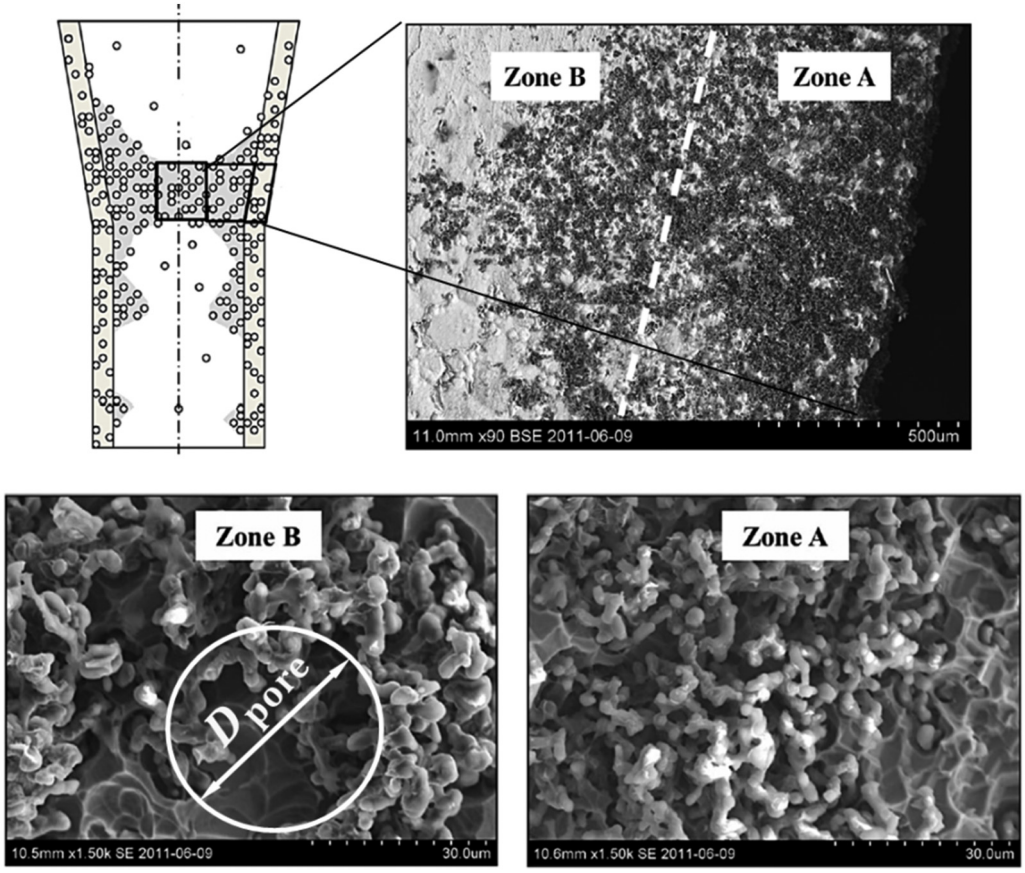

Fig. 4. Metallographic analysis (SEM) of the clog material (alumina) in the nozzle of a pilot experiment [29]. Copyright 2015 with permission from John Wiley and Sons.

for building the clog growth model. The growth of the clog is governed by the deposition of NMI particles. One assumption is that particles reaching the clog front completely stick (100% sticking probability), with no detachment and no fragmentation phenomenon occurring.

In order to describe the algorithm of clog growth, another quantity is introduced: f_{clog}, As shown in Fig. 5, f_{clog} describes the fraction of the volume which is occupied by the clog in the local computational cell. Additionally, following cell markers are defined:

1. All computational cells, including the boundary cells which are adjacent to the nozzle wall, are initially marked as 'white' cells. NMI particles can only possibly deposit on the wall (Fig. 5(a)). The wall is gradually covered by the deposited particles, initiating the clog growth. f_{clog} increases from 0.0; the algorithm for the early stage of clogging, corresponding to the step (a) of Fig. 1, is described in §2.3.
2. When the clog in a boundary cell grows over half of the cell ($f_{clog} = 0.5$), the boundary cell is marked as 'yellow' (Fig. 5(b)). Inside yellow cells, growth of the clog occurs, and f_{clog} increases continuously with the progress of the deposition of NMI particles on the clog front. f_{clog} increases from the initial value of 0.5 to 1.0 in the boundary cells.
3. When f_{clog} reaches 1.0, the cell marker converts into 'red'. The face-bonded neighboring cells (Fig. 5(c)) are marked as 'yellow'. The clog continues to grow in the yellow cells. Inside the red cells, the average solid volume fraction of the clog ($\overline{f}_p$) remains constant.

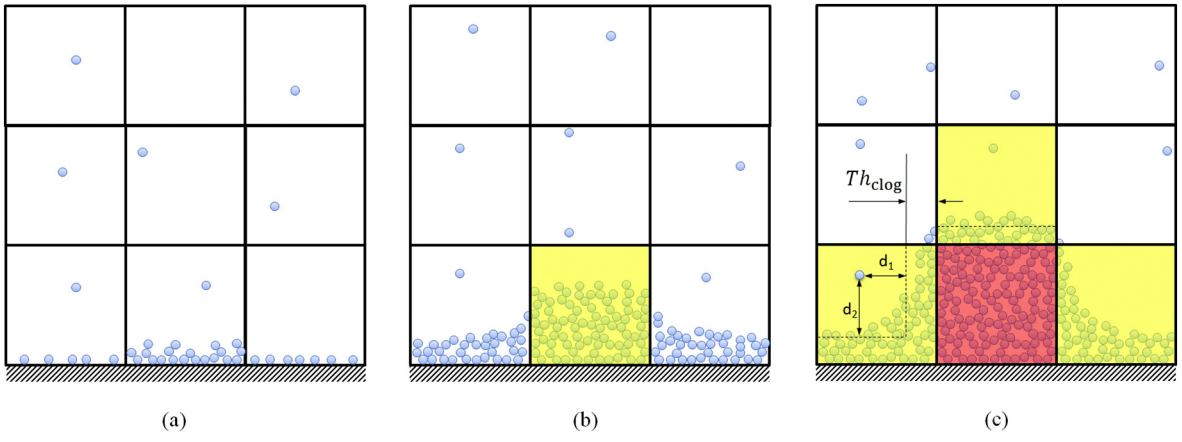

Fig. 5. Origin and growth of the clog: (a) initial deposition of particles on the wall, (b) start the growth of the clog, (c) continuous growth of the clog into the bulk region.

Making a decision on how a particle adheres to the clog front in a yellow cell depends on its distance to the clog front (Fig. 5(c)). The clog front (dash line) is calculated by assuming there is a uniform distribution of clog on mutual faces with neighboring red cells or nozzle-wall in a yellow cell. In other words, the clog volume in a yellow cell is divided by the total area of mutual faces with a neighboring red cells or wall. Thus, uniform thickness of the clog in a yellow cell is assumed, as in the following equation:

$$Th_{\text{clog}} = \frac{f_{\text{clog}}\,\Delta V}{\sum A_{\text{face}}}, \tag{17}$$

where ΔV is the volume of the cell, and A_{face} is the clog face area of the cell.

After a particle enters a yellow cell, its distances from the clog front are calculated. If the minimum distance is smaller than the radius of the particle ($d_p/2$) it will adhere to the clog front. The volume of the clog increases by $\pi d_p^3/(6\bar{f}_p)$ in the yellow cell and the particle is no longer considered in further calculations. This procedure is shown in the flowchart of Fig. 6.

To incorporate the porous structure of the clog in flow calculations, we require the permeability of the clog. The permeability is treated as a function of the average solid volume fraction of clog $\bar{f}_p$, the diameter of large pores D_{pore} and the fraction of clog in the considered cell f_{clog}.

$$K_{\text{per}} = \frac{\left(1-\bar{f}_p\right)\left(1-\bar{f}_p^{\,1/3}\right)}{108\left(\bar{f}_p^{\,1/3}-\bar{f}_p\right)} D_{\text{pore}}^2 \frac{1}{f_{\text{clog}}^n}, \tag{18}$$

where n is an interpolation correction power. The above expression is a modified equation of what was presented by Yang [54] for isotropic porous media with large open pores. For denser porous clog conventional Kozeny–Carman equation for packed bed of spheres, $K_{\text{per}} = (d_p^2/180)(1-\bar{f}_p)^3/\bar{f}_p^2$, can be applied.

Then, Darcy source terms for the clog region are defined as below for $\vec{u}$, k, and ω, respectively.

$$\bar{S}_u = -\frac{\mu}{K_{\text{per}}}\vec{u} \tag{19}$$

$$S_k = -\frac{\mu}{K_{\text{per}}}k \tag{20}$$

$$S_\omega = -\frac{\mu}{K_{\text{per}}}\omega \tag{21}$$

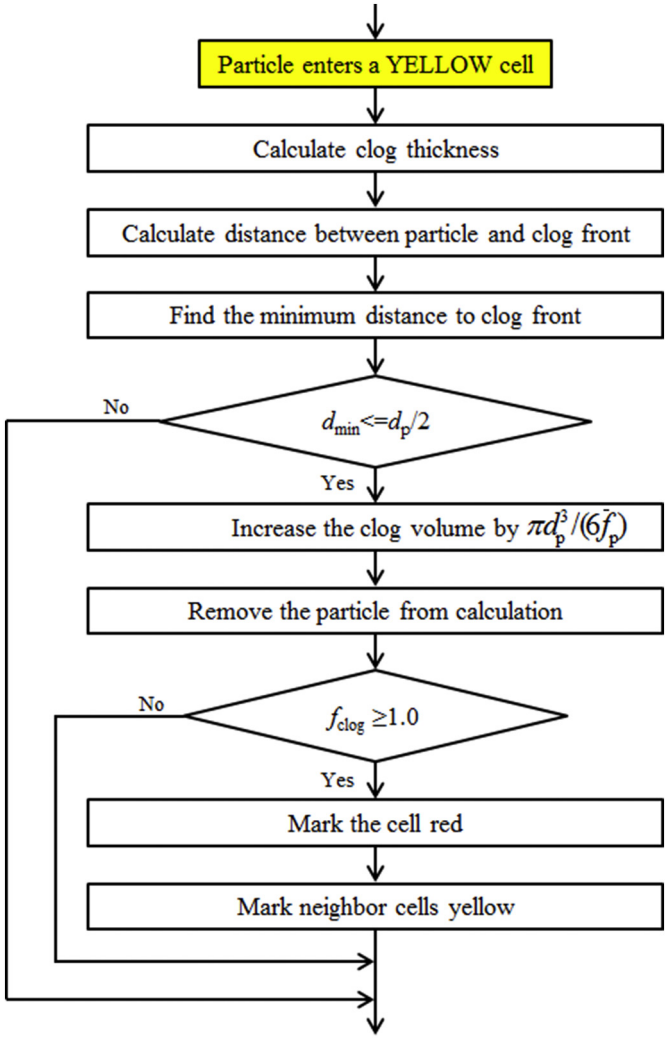

Fig. 6. Flowchart for clog growth.

3. Validation

3.1. Benchmark

A laboratory device as used to investigate the nozzle clogging (Fig. 7(a)) is simulated [12,29,53,55,56]. This device is made from a pilot scale induction furnace and a circular nozzle as situated at the bottom of the furnace. The nozzle is heated to a temperature above the melting point of the melt, to prevent the nozzle from freezing during the run of the experiment. Steel is melted in the induction furnace and deoxidized with aluminum. After a certain holding time for de-oxidation, the nozzle is opened and the molten steel flows through the nozzle. The melt is poured into a container from the nozzle. The mass flow rate is dynamically monitored by weighing the mass of the steel as it is collected by the container. The poured melt is exposed to air and the oxidation of the melt might affect the measurement of the mass flow rate. However, an experimental study on oxidation rate of molten steel [57] showed that the oxidation rate in the still state is controlled by the diffusion of oxygen in the oxide film and in the stirred state is controlled by the diffusion of oxygen in the gas phase. In both cases the diffusion is a very slow step; therefore, the effect of the melt oxidation on the weight measurement is negligible.

Dimensions of the computational domain with enmeshment are shown in Fig. 8. A finer mesh is generated in the nozzle region where clogging may occur. The minimum cell size, 5.63×10^{-12} m^3, is located near the nozzle wall; the maximum cell size, 1.3×10^{-5} m^3, is located in the furnace.

A volume of fluid (VOF) method is applied to calculate the two-phase (melt and gas) flow. In laboratory experiments using this device, liquid argon is added to provide an Ar atmosphere in the furnace in order to prevent any possible re-oxidation of the steel. However, here, simply the density and viscosity of air are taken for the gas phase, like the previous simulation for this device [56]. On the top surface of the furnace, a pressure-inlet boundary condition with atmospheric pressure is set for the air. For the nozzle outlet, a pressure-outlet is applied for the melt flow. Non-slip boundary conditions are valid on all other walls. 350 kg of steel melt is filled in the furnace before running the experiment. To this end, the melt height is 0.275 m and there is a layer of air 20 mm thick on top of the melt. The velocity, turbulence kinetic energy k, and specific dissipation rate ω are set to zero as initial conditions. The melt drains through the nozzle by gravity, and the air continuously

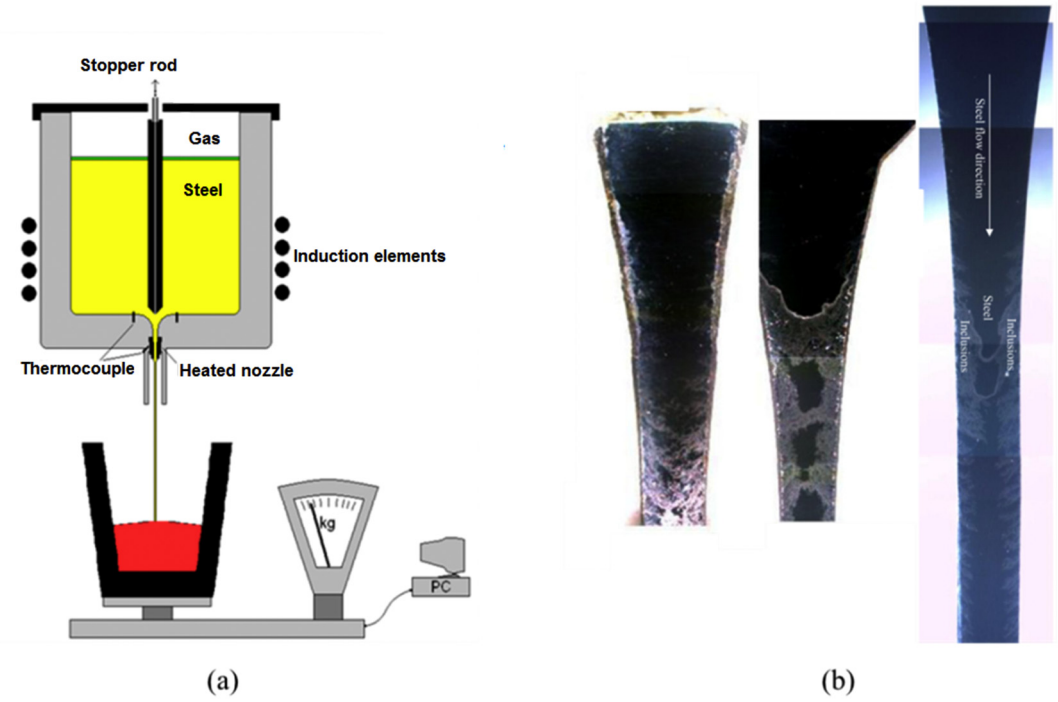

Fig. 7. Schematic of a laboratory device to investigate the clogging (a) and typical macrographs of as-clogged nozzle (b). The narrowest part of the nozzle has a diameter of 5 mm. Copyright 2011 with permission from Taylor & Francis.

flows in through the pressure-inlet. The initial roughness height on the nozzle wall is 2×10^{-5} m, which increases as the particles deposit.

To save computation time and avoid redundant calculations of particle tracking in the furnace, particles are injected on the connection plane between the bottom of the furnace and the top of the nozzle, as shown in Fig. 8. A previous simulation has demonstrated that particle distribution in the induction furnace is quite uniform due to two reasons. Firstly, the melt is agitated by electromagnetic force. Secondly, the particle size is only a few micrometers. The drag force of the melt on the particles is dominant; hence particles follow the melt flow in the bulk of the furnace. The particle mass-injection-rate is set proportionally to the mass flow rate of the melt. When the mass flow rate of the melt decreases due to clogging, the particle mass-injection-rate is reduced proportionally. The diameter of each particle is set at 3 μm regarding the average diameter of alumina inclusions as reported in [29]. Since accurate mass-injection-rates are not available, it is assumed to be ~9.79×10^{-6} kg/s initially as a suitable parameter; this value is discussed in §5.

Physical properties of different phases (steel melt, alumina particles, and air) and other parameters as required by the model are listed in Table 3. A full 3D calculation is made and the numerical model is implemented in the commercial CFD code ANSYS-FLUENT 14.5 with the extended user defined functions (UDFs) for considering the particle motion near the wall and the clog growth. Shear-stress transport (SST) k-ω model is used to model turbulent flow which effectively blends the precision and robustness of k–ω model in the near-wall region with the bulk liquid k–ε modeling in the far field. A key point of this model is insensitivity of flow to grid spacing near the wall. A detailed explanation can be found in [58,59]. The absolute convergence

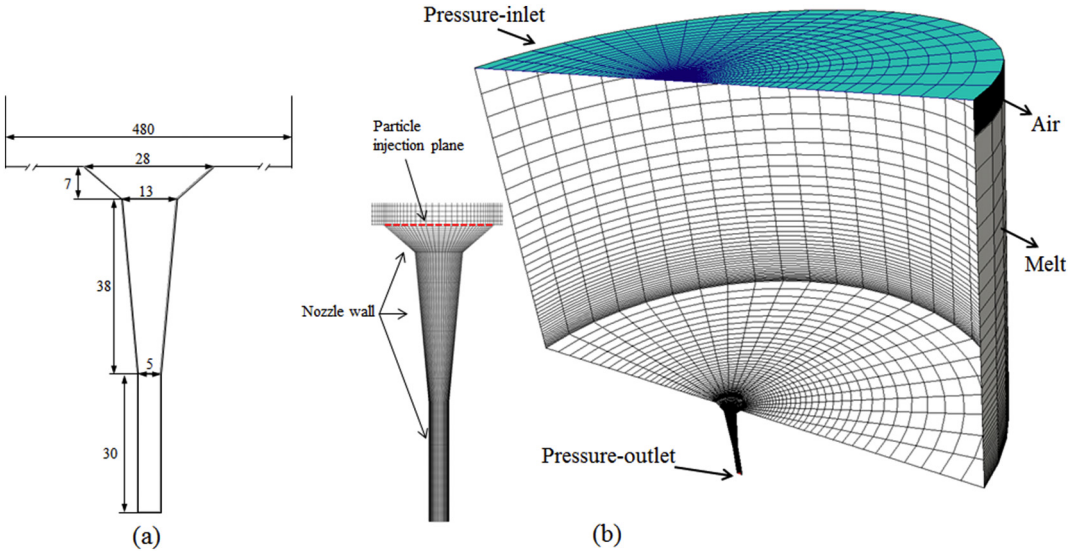

Fig. 8. Dimensions in mm of the computational domain (a) and illustration of the mesh with boundary conditions (b).

Table 3
Physical properties, process and numerical parameters.

Property	Unit	Value
Density		
Steel melt	$kg.m^{-3}$	7020
Alumina (sold)		3700
Air		1.225
Viscosity		
Steel melt	$kg.m^{-1}.s^{-1}$	0.006
Air		1.7894×10^{-5}
Time step for flow	s	0.01
Lagrangian time scale (T_L)[a]	s	1.0×10^{-5}
Average volume fraction of solid particles ($\overline{f}_p$)[a]	–	0.5
Pore diameter in clog (D_{pore})[a]	m	3.0×10^{-5}

[a] Parameters are varied in verification simulations.

criteria for all transport equations are set to 1×10^{-4} and the under-relaxation factor is 0.3, 0.5, 0.8, and 0.8 to solve equations of continuity, momentum, k, and ω, respectively. Time step size is defined as 0.01 s during the simulation. Computation is done on a high-performance computer cluster with 6 CPUs (2.9 GHz), and the computation for each simulation takes approximately 6 days.

3.2. Results

The flow pattern before injecting the particles is depicted in streamlines (Fig. 9(a)). At this moment, the nozzle wall is considered to be 'clean', i.e. the wall has only the initial wall roughness without any particle deposition on it. In Fig. 9(b)–(c), the velocity magnitude and turbulence kinetic energy contours are presented on a symmetry plane before and after clogging, respectively. Prior to clogging, the melt flows smoothly through the nozzle. Turbulence begins to appear from the upper part of the nozzle and becomes stronger along the nozzle wall with the gradually-converged nozzle section. After clogging, the striking feature of the flow pattern is the dramatic increase in turbulence with incremental clogging. The maximum velocity does not alter significantly, it even drops slightly. However, the turbulence kinetic energy increases by 5 orders of magnitude in the lower part of the nozzle due to the bumpy clog front and the reduced cross-section of the flow passage (Fig. 9(c)).

Possible trajectories of particles are displayed in Fig. 10. Two different scenarios are analyzed: one is the early stage and the other is the later stage of clogging. During the early stage of clogging, the nozzle wall is 'clean' with its initial wall roughness, or it is only covered by few deposited particles. This early stage clogging is referred to as the change of the wall roughness height. During the later stage, the growth of the clog is considered, i.e. the front of the clog is tracked explicitly.

Illustratively, three particle trajectories are selected, representing three different fates of the particles.

(1) A particle can follow the bulk turbulent flow and exit from outlet.
(2) A particle is initially transported into the turbulent boundary layer near the wall. Due to the interactions between the coherent flow structures and the particle, the particle is 'ejected' from the wall and returns to the bulk flow [45]. Trajectories of particles, which pass the boundary layer, are represented in green.
(3) A particle is firstly transported into the turbulent boundary layer near the wall and then adheres to the wall. Due to the interactions between the coherent flow structures and the particle, the particle is propelled towards the wall by the 'sweep' action [45].

Similarly, three scenarios for particles exist during the late stage of clogging (Fig. 10(b)). The clog region is represented in yellow, and the trajectories are shown in blue lines. No turbulent boundary layer can be determined near the front of clog. However, a numerical treatment is performed for the volume element which includes the front of clog. Here the portion of the trajectory is also marked in green when a particle enters the volume element of clog front. A particle entering this clog front element adheres to the clog front, or returns to the bulk flow, depending on the minimum distance the particle can reach the clog front.

Evolution of clogging is depicted in Fig. 11(a). At 50s, the narrowest section and a portion of the middle section of the nozzle are covered by a smooth layer of clog. In these sections, the flow near the wall has the largest turbulence kinetic energy (Fig. 9(b)), which promotes the transverse motion of particles. It appears to be erratic as to where the particle deposition occurs in the middle section. Note that individual particles or tiny amounts of particles deposited on other the uncovered wall of the nozzle may not at all be visible in Fig. 11. With the continuous deposition of particles on the nozzle wall, the clog starts to grow and some

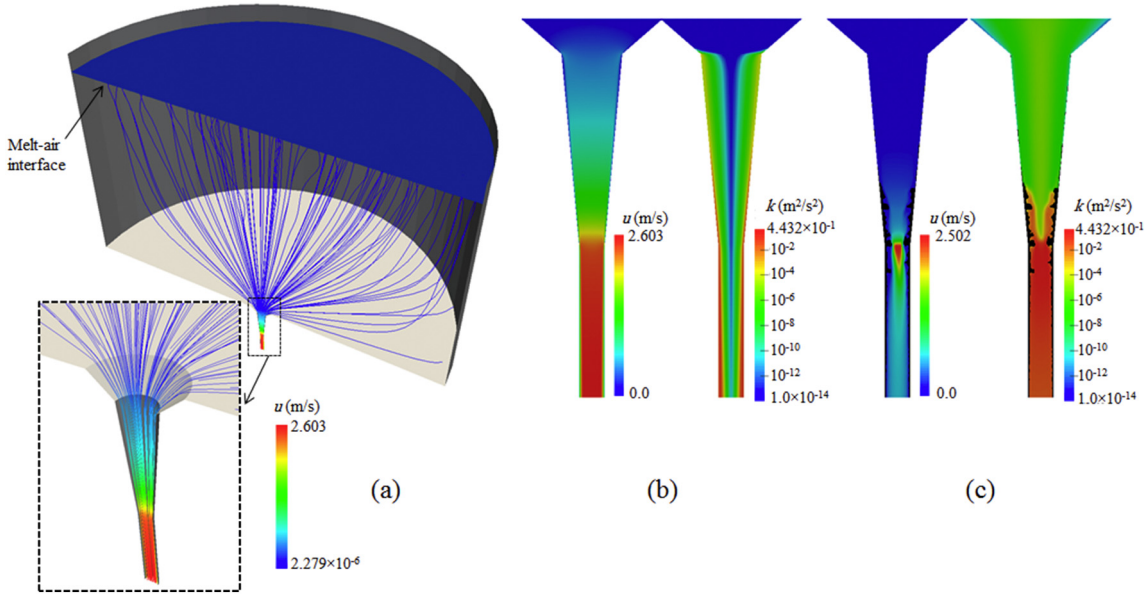

Fig. 9. Characteristics of the flow patterns with and without considering clogging. (a) Flow pattern in streamlines; (b) velocity magnitude and turbulence kinetic energy of the melt in the nozzle without considering clogging; (c) velocity magnitude and turbulence kinetic energy of the melt in the nozzle considering clogging (200 s after particle injection). The velocity magnitude is shown with color in linear scale, while the turbulence kinetic energy in logarithmic scale. In the case considering clogging, the clog is shown in black.

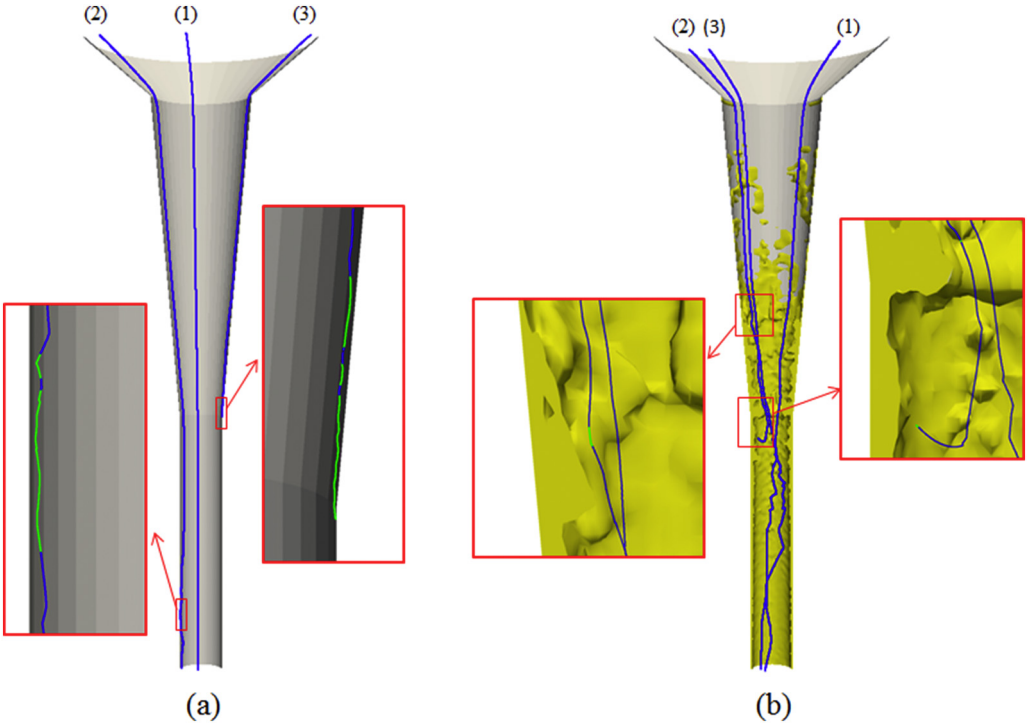

Fig. 10. Trajectories of particles in the initial stage (a) and later stage of clogging, i.e. 200 s after particle injection (b). Trajectories of three particles are selected to illustrate their different fates: (1) passing through the nozzle with the bulk melt; (2) being transported in the near-wall or partially clogged region, then returned into the bulk melt; (3) being transported in the near-wall or partially clogged region, then adhering to the wall or the clog front. The trajectory of the particle in near-wall or partially clogged region is highlighted in green. (For interpretation of the references to color in this figure legend, the reader is referred to the web version of this article.)

asperities of the clog front can be seen in the period between 100 and 150 s. Snapshots at 200 and 250 s show some bulges of the clog, which grow much faster than those in neighboring regions, and a branched structure develops to a certain degree. These branched structures are more pronouncedly visible in the transition region between the middle section and the narrowest section of the nozzle. Finally, the branched clogging structures now grow continuously until they meet in the nozzle center, and the cross-section of the nozzle is blocked. In Fig. 11(b) a zoomed view of clog, overlaid with the flow field in streamlines, is displayed at 200 s. It demonstrates that the formation of the irregular clog front adapts the flow field (streamlines), leading to the formation of eddies. As a result, the adapted flow field influences the trajectories, hence the 'fates' of the particles. For example, the eddy under the necking area causes the trajectory of the particle (3) to bend upwards (Fig. 10(b)). The particle rises and then adheres to the clog front.

The total mass of the clog, i.e. the mass integral of particles as deposited on the nozzle wall and on the clog front, and the deposition rate are

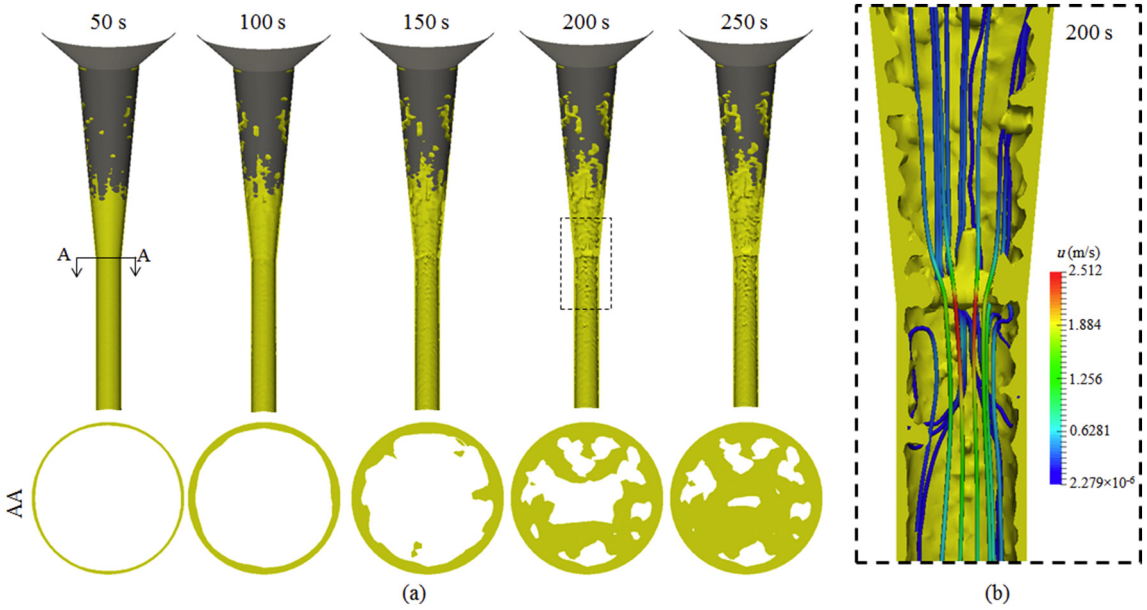

Fig. 11. Evolution of clogging in the nozzle. (a) View of the clog region from the vertical section and a cross-section A-A of the nozzle; (b) Zoomed view of the flow streamlines and a partially clogged section at 200 s. The clogged section is shown in yellow. The magnitude of the flow velocity is shown in a color scale along the streamlines. (For interpretation of the references to color in this figure legend, the reader is referred to the web version of this article.)

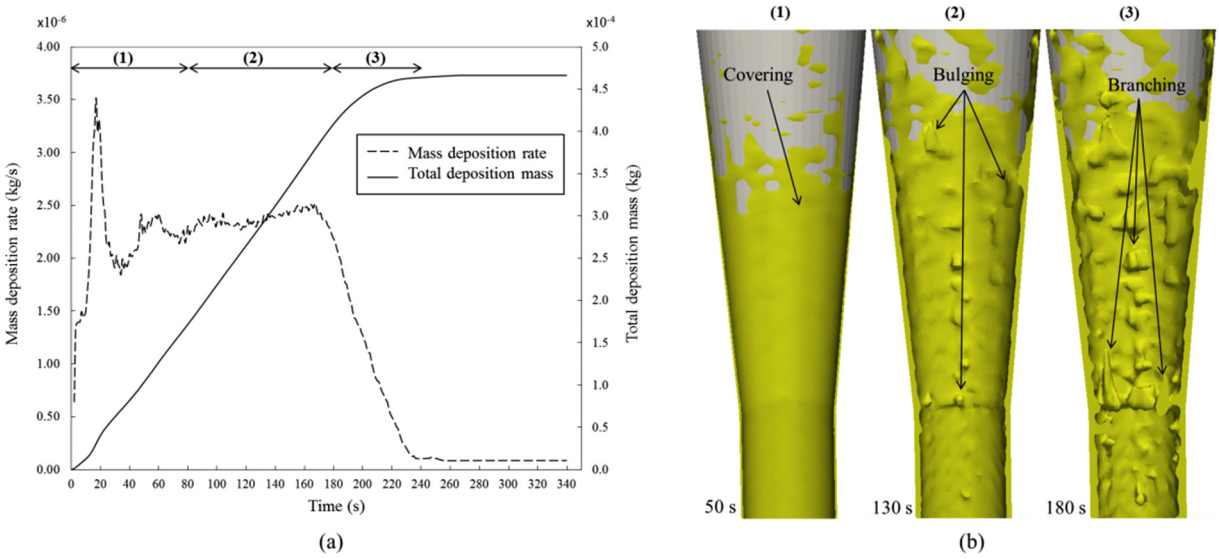

Fig. 12. Numerically calculated total mass of the clog, i.e. the mass integral of particles as deposited on the nozzle wall and on the clog front, and the mass deposition rate are plotted as functions of time (a). Three periods of clogging evolution are indicated (b): (1) initial covering of the nozzle wall by the deposited particles, (2) developing a bulged clog front, and (3) developing the branched clog structure.

plotted as functions of time in Fig. 12(a). The curve of the total particle deposition mass appears relatively smooth, but the mass deposition rate varies significantly. This variation coincides with the aforementioned periods of clogging, as shown in Fig. 12(b). (1) The initial covering of the nozzle wall by the deposited particles. The deposition rate increases initially, then decreases and fluctuates until 80 s. (2) The build-up of the bulged clog front. The deposition rate is almost constant with minor fluctuations. This period lasts from 80 to 180 s. (3) The build-up of the branched structures of clog. The deposition rate decreases rapidly. This period starts at about 180 s, ending with complete blockage of the nozzle. Totally, ~34% of the injected particles entering the nozzle attach to the wall/clog and stop the flow after about 250 s.

3.3. Comparison with experimental data

The numerically predicted clogged nozzle, shown in Fig. 11, is qualitatively comparable with typical as-clogged cross-sections of the nozzle from laboratory experiments (Fig. 7(b)). The total mass and the mass flow rate of the steel melt as drained-out from the nozzle are measured experimentally, and they are plotted as functions of time [29]. A Comparison with the numerically simulated results is made in Fig. 13. Generally, the tendencies of the experimental curves are well-predicted by the numerical simulation, but the details of the experimental curves are still not ideally 'reproducible'. For example, the model underestimates the mass flow rate for the first 60 s, overestimates it between 60 and

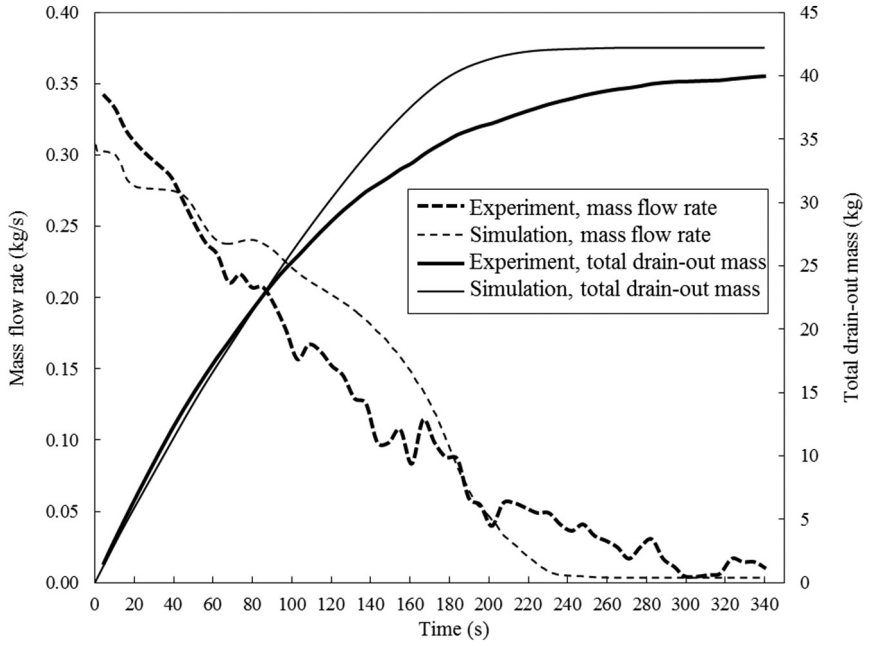

Fig. 13. The total mass and the mass flow rate of the steel melt as drained from the nozzle are measured and plotted as functions of time [29]. They are then compared with the numerically simulated results.

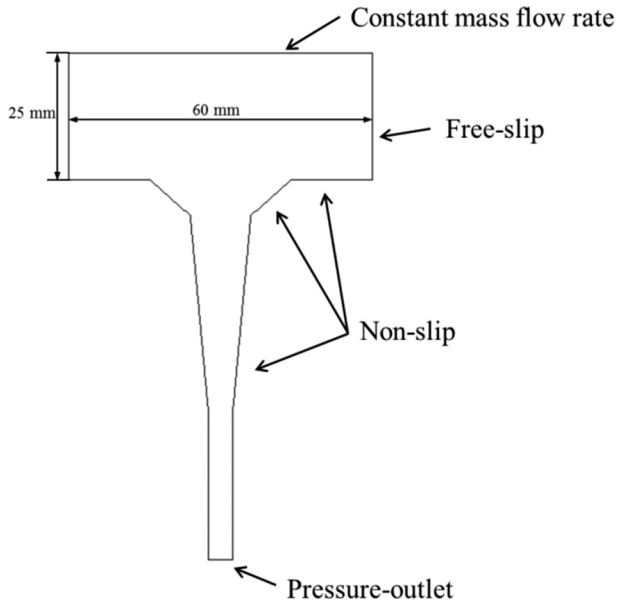

Fig. 14. Geometry and boundary conditions of the calculation domain are adapted for the purpose of model verification.

180 s, and again underestimates it after 200 s. One reason for this deviation is the model's inaccuracy, but it is also noteworthy that the experimental data was obtained by measuring the force as applied by the exiting melt on the container (Fig. 7(a)). The momentum impact of the falling melt stream is ignored in this experiment. Additionally, the model might overestimate the clogging. As seen from Fig. 13, the nozzle is predicted to be fully clogged at about 230 s, while the experiment shows that the mass flow through the nozzle does not halt until around 300 s.

4. Verification

To facilitate the model verification, a reduced calculation domain was taken into account, as shown in Fig. 14. Correspondingly, a free-slip condition for the side wall and a constant mass flow rate for the inlet at the top surface are applied. The nozzle's geometry and the boundary conditions for the nozzle walls remain unchanged (Fig. 8). With these simplifications, no air phase is involved. The initial roughness height of the nozzle wall is 2×10^{-5} m. The mass flow rate for the melt at the inlet is 0.3 kg/s, the same as the initial mass flow rate in the laboratory experiment (Fig. 13). Particles with a mass rate of 5.02×10^{-5} kg/s and a diameter of 5 μm are injected onto a horizontal section, 10 mm above the nozzle. Note that these special boundary conditions and settings have been designed for the purpose verifying this model, and they are not compatible with the previous experiment.

4.1. Mesh size sensitivity

Different mesh sizes have been created for this study, and distribution of the mesh is not homogenous in the computational domain. The near-wall region is the most important, hence the finest mesh, as noted by its cell thickness (mm), is adjacent to the nozzle wall. Four cases have been calculated with a minimum cell thickness of 0.06, 0.08, 0.10 and 0.15 mm, respectively.

In Fig. 15(a), the total particle deposition mass as a function of time is evaluated. With the special setting of this benchmark, i.e. imposed constant mass flow rate of the melt, two typical changes of the curvature of the curves are evident: the first change is at ~2 s and the second one is at around 42–46 s. The first change corresponds to the early stage of clogging, while the second corresponds to the morphological transition of the clog front from the bulged front to the branched structure (Fig. 15(b)). During the early stage of clogging, the case with the largest mesh size, 0.15 mm, appears to calculate more deposition mass, while results of other cases, mesh sizes ≤0.1 mm, are similar, i.e. their curves are close to each other until 24 s. The growth of the clog front (Fig. 15(b)) in the case with the coarsest mesh is also significantly divergent from other cases. Therefore, based on similar results of cases with mesh size ≤0.08 mm, we suggest that the case with smallest mesh size of 0.08 mm adjacent to the nozzle wall is sufficient to solve the clogging problem during the early stage; this mesh size is also selected for other simulations. There is a substantial difference between the four degrees of mesh fineness observed during the late stage of clogging (after the bulge-branch transition). We should mention that a relatively coarse

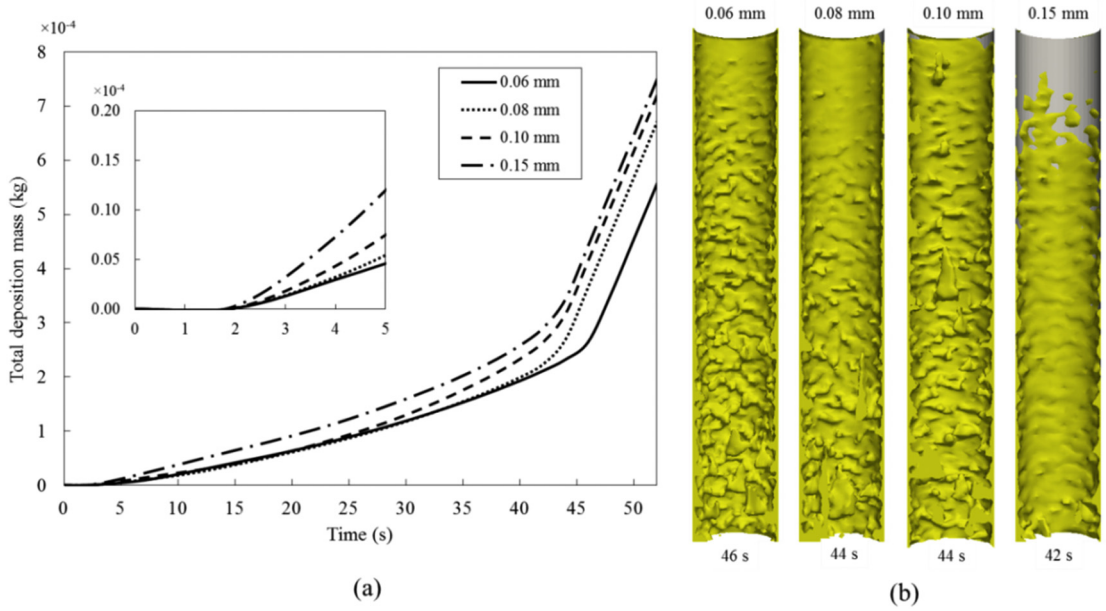

Fig. 15. Sensitivity of the calculated total particle deposition mass in relation to the mesh size. Four calculations with a different mesh fineness, respectively, are calculated and compared. Values in the legend stand for minimum cell thickness adjacent to the nozzle wall. (a) Total particle deposition mass as a function of time; (b) Clog front profile as predicted at the moment of branching.

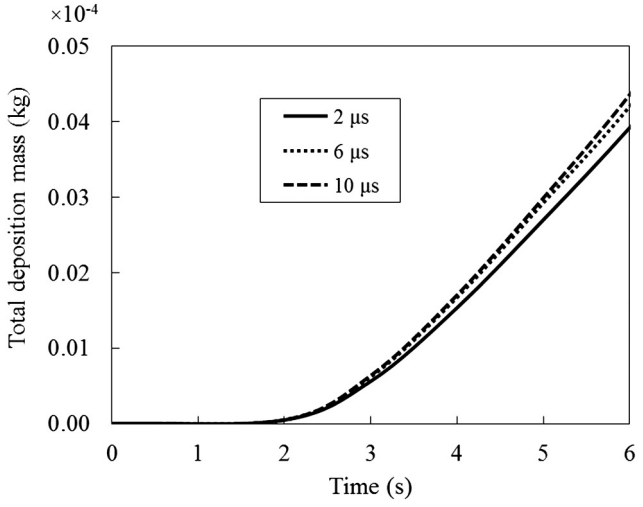

Fig. 16. Influence of the Lagrangian time scale (T_L) on the total particle deposition mass.

mesh size (~3 times larger than the smallest mesh size adjacent to the nozzle wall) is used in the interior of the nozzle. These coarse mesh sizes might not be sufficient to solve the late stage of clog growth precisely.

4.2. Lagrangian time scale

The Lagrangian time scale (T_L) is a numerical parameter which is used in the stochastic model of particle tracking in the turbulent boundary layer. Results of the total deposition mass of particles for different values of T_L (2–10 μs) are evaluated in Fig. 16. Since T_L is applied only for the early stage of clogging, the curves are plotted until 6 s. It shows that three values of T_L lead to similar deposition mass. The value of 2 μs T_L leads to a slightly smaller amount of deposition, meaning there is a prediction of the smaller deposition mass. To confirm this finding, a further study of the effect of T_L is to be performed. In a wall-bounded cell at 0.03 m from the outlet, 1000 particles are injected at identical time and position. We track the fates of these particles by using different T_L (2, 6, 10 μs). The model is inherently stochastic and results of one simulation trial are different from those of others even same settings are made. Therefore, for each T_L the simulation is repeated 10 times and then average values are compared. According to the new results, as shown in Fig. 17, the number fraction of particles (in percentage) as adhered to the wall for the cases with $T_L = 6$ and 10 μs are almost the same, whereas, for the case with $T_L = 2$ μs, it is ~0.5% smaller. Again, it transpired that the case with $T_L = 2$ μs predicts the smaller deposition mass. The standard deviation for the 10 times of repeated calculations, identified by error bars, is also shown in Fig. 17. The standard deviation seems to increase with T_L. Therefore, T_L should not be too large, which is the subject of further discussion in §5.

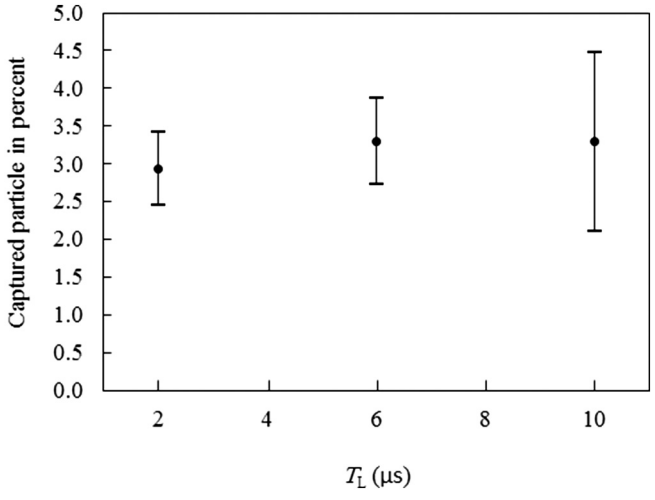

Fig. 17. Influence of the Lagrangian time scale (T_L) on the number fraction of particles that adhere to the wall. Error bars represent standard deviation.

4.3. Correction power

In the current model, according to the postmortem analysis of the clog structure [29], clog is assumed to be a uniform, isotropic, porous medium. In a partially clogged cell, the average permeability is calculated as:

$$K_{per} = \frac{\left(1-\bar{f}_p\right)\left(1-\bar{f}_p^{1/3}\right)}{108\left(\bar{f}_p^{1/3}-\bar{f}_p\right)} D_{pore}^2 \frac{1}{f_{clog}^n}, \tag{22}$$

where n is the correction power. For a fully-clogged cell, n plays no role. In Fig. 18(a) $1/K_{per}$ as a function of f_{clog} is plotted for different n's. $1/K_{per}$ is used to calculate a Darcy source term in momentum, k, and ω equations. A value of 1 for n means a linear interpolation of $1/K_{per}$ between $f_{clog} = 0$ and $f_{clog} = 1$. In this case, a very small change of f_{clog} initially would lead to an immediate increase of $1/K_{per}$. In other words, with a small amount of particle deposition in a new computation cell, the permeability of this cell decreases rapidly. This, however, does not make sense physically. Thus, a larger value for n should be selected. In Fig. 18(b), total deposition mass vs. time is shown for different values of n (1, 2, 5, 10). Logically, until 35 s, there is no difference to be identified between the different cases, as the formulations for permeability (Eq. (22)) influence only the inner region of the clog. Substantial deference is evident during the late stage of clogging after the bulge-branch transition and a greater value of n results in earlier branching.

4.4. Porosity

The porosity of clog material is described by the process parameters, d_p, $\bar{f}_p$ and D_{pore}. They must be determined experimentally. Since $\bar{f}_p$ and D_{pore} are related to each other and one of them cannot change independently, as listed in Table 4, three sets of $\bar{f}_p$ and D_{pore} are suggested (Case 1–3). The porosity parameters of Case 2 are used for previous verification studies (§4.1–4.3). For Case 4, the assumption of there being an open pore structure is not valid. Therefore, in Case 4 the porous medium is assumed to be formed with randomly packed spheres, for which the Kozeny-Carman permeability law is applicable. For all cases, $d_p = 5$ μm. Particle deposition mass is presented in Fig. 19(a). Clog front morphology at the moment of bulge-branch transition is shown in Fig. 19 (b). Observations show that while for Case 1–3 bulge-branch transition happens at 36, 44, and 46 s, respectively, Case 4 shows no sign of this transition until 60 s. The deposition rate prior to the bulge-branch transition, i.e. slope of the curve of deposition mass, increases with $\bar{f}_p$.

5. Discussion

In various fields of study, critical steps of clogging (Fig. 1) have been investigated, as recently reviewed by Henry and co-workers [6,60], but most available numerical models are valid only for one individual clogging step or combine two steps, and the dynamic growth of the clog and its influence on the flow were ignored. To the authors' knowledge, only one recent work has reported a model which has considered the aforementioned three steps [40]. Similarly, the step of resuspension or fragmentation (Fig. 1(d)) was not included. Most significant innovations of the current model are as follows.

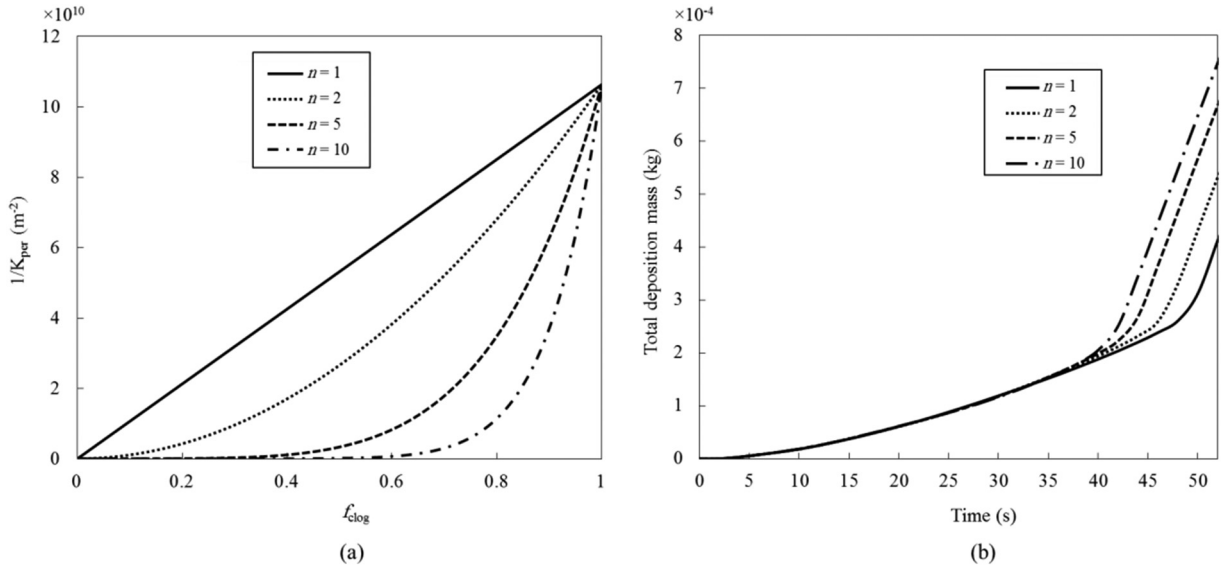

Fig. 18. Influence of the correction power in the permeability formulation on the total deposition mass. (a) $1/K_{per}$ as a function of f_{clog}; (b) total deposition mass as a function of time.

- Turbulence near the wall determines clogging initialization or deposition of the first layers of particles. The dynamic change of wall roughness by the initial deposition of non-metallic inclusions (NMIs) on the wall is incorporated into the model, which influences the flow field and turbulence. Therefore, a model considering two-way coupling between particle deposition and fluid flow is provided for the early stage of clogging. If the wall-bounded cell size is much larger than the particle size, a long time is needed to particles occupy half of the cell, and form a porous medium. Therefore, there is a noticeable delay in the effect of clogging on the flow pattern. Using the dynamic change of wall roughness would overcome this problem and would help to mimic the transient behavior of clogging.
- A new clog growth algorithm on the base of volume average approach is proposed. The clog front is explicitly tracked with a cell marker. The progress of the clog front is governed by continuous deposition of NMIs at the clog front, i.e. in the cells of clog front. According to the volume fraction of the clog in the cell, volume averaged permeability is applied to treat the interactions between the clog and the flow.
- A formulation for isotropic porous media with open pores [54] is employed to calculate permeability of the clog. It is more compatible with the clog structure as observed experimentally (Fig. 4) than what has been assumed with morphology of homogenously packed spheres. The later may overestimate pressure drop in the clog.
- A volume average interpolation is used to find permeability in the partially-clogged cells (clog front cells). This method is more reliable than simply considering the clog front cell as a uniform porous medium with actual solid fraction (f_p). We have verified that a simple treatment (considering the clog front cell as a uniform porous medium) would lead to an unrealistic modeling result by overestimating the drag effect of the clog front on the flow. Note that the flow near the clog front will directly influence the deposition rate of the NMIs.
- Using the volume average approach for clog growth, the requirements on computational resources will diminish. Demands on computational resources are often a limiting factor for most clogging models, especially for industrial cases.

Table 4
Properties of porosity in different cases.

	$\overline{f}_p$	D_{pore} (μm)
Case 1	0.400	60
Case 2	0.500	50
Case 3	0.550	45
Case 4[a]	0.634	–

[a] For this case Kozeny-Carman permeability is used.

Simulation results have demonstrated the model capabilities for clogging. Different stages of clogging including the clog-flow interactions are to be considered: (1) calculation of particle trajectory with emphasis on near-wall region; (2) deposition of particle based on its distance to the wall or clog front; (3) effect of the initial wall roughness and dynamic adaptation of the wall roughness due to particle deposition at the early stage of clogging; (4) growth of the clog as porous material due to particle deposition; (5) effect of clogging on fluid flow accordingly in the early stage (by change in wall roughness), and in the later stage (by applying Darcy source term). The numerical model provides a valuable tool to achieve a deeper understanding of clogging, which would never be realized experimentally. The model verifies that clogging is a highly transient, stochastic and self-accelerating process.

The as-clogged nozzle section obtained by simulation is similar to typical experimental ones. The experiment demonstrates that small spherical inclusions tend to deposit on the narrow passage of the nozzle [12,55], and this is well 'reproduced' by the model, as can be seen in Fig. 11. We, therefore, claim that the model is able to predict the clog growth qualitatively sufficiently well. A quantitative comparison of melt flow rates between the simulation and experimental results exhibits some differences (Fig. 13). For instance, in the simulation the flow is stopped by clogging sooner than was the case in the experiment. In the final step of the clogging, after clog branches begin to develop, only small holes are left in the clogged nozzle-section, as depicted in Fig. 11(a). Owing to the fact that the current mesh size (as limited by the computer hardware) is not able to resolve the holes precisely, the melt flow is blocked earlier in the simulation than it does in reality. In addition, mesh sensitivity investigation (Fig. 15(a)) shows that in the later stage of clogging, when the clog is growing, a coarser mesh renders an earlier bulge-branch transition. We anticipate that if the mesh is fine enough to resolve the clog front properly, the time of nozzle blockage will be later,

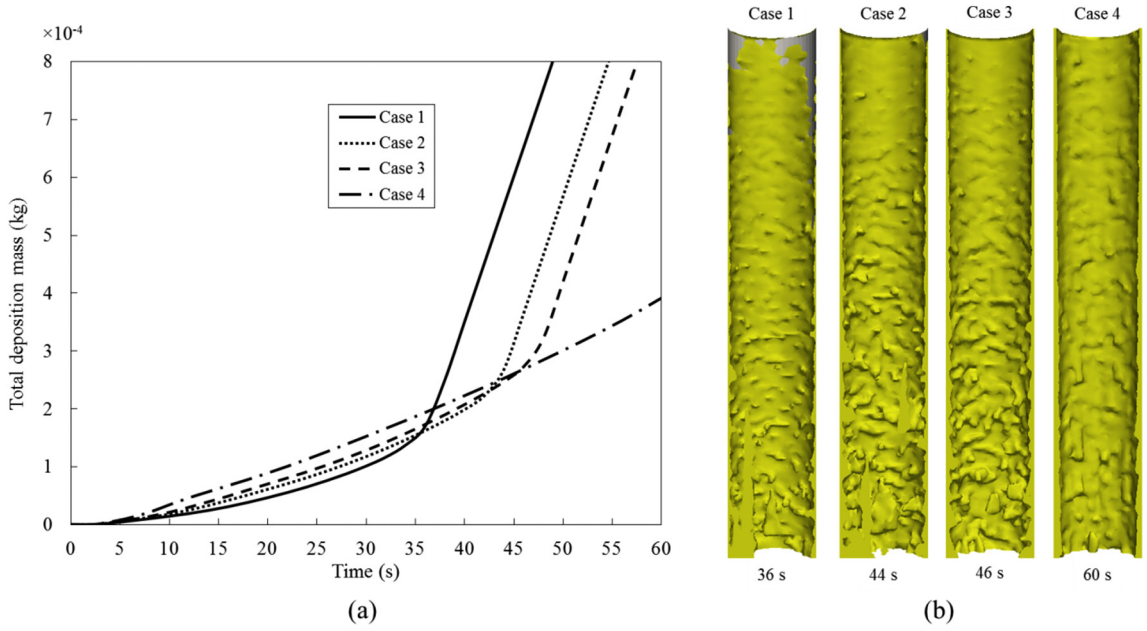

Fig. 19. Influence of porosity parameters of the clog on the total particle deposition mass and the clog front morphology. (a) Total particle deposition mass as a function of time and (b) clog front morphology for four different cases as defined in Table 4.

closer to what is the case in reality. Another reason for the inaccuracy in the calculation might be due to the volume average method. This method is not oriented to the structural details of the clog at the microscopic scale, but to a reasonable approximation of the clog growth.

The particle deposition rate is definitely related to the particle number density in the melt, i.e. the particle mass-injection-rate, as set in the model; a higher mass-injection-rate leads to faster clogging. The value for the particle mass-injection-rate used in the validation simulation, ~9.79×10^{-6} kg/s, is around 67 times smaller than what was obtained from the melt analysis during the experiment [29], ~6.55×10^{-4} kg/s. Applying the experimental values in the model leads to rapid blockage of the nozzle, therefore, it is not applicable to the simulation. According to the data from a steel plant for ULC IF steel grades [61], the mass fraction of alumina inclusions in the steel melt would be 4.25×10^{-5}–8.5×10^{-5}, while the mass fraction of alumina inclusions was ~7.3×10^{-3} for the laboratory experiment [29]. It illustrates that reported values of the number density of inclusions in the laboratory experiment, extracted from melt samples, may be calculated inaccurately or they do not represent the number density of inclusions which enter the nozzle. The mass fraction of inclusions in the simulation is 3.26×10^{-5}, which coincides well with the data from the steel plant. From an alternative perspective, in the current model, the sticking probability of a particle when it reaches the nozzle wall or clog front is considered to be 100%. This assumption may underestimate the number density of inclusions required to block the nozzle. Therefore, deeper investigations and more robust evidence are going to be required to ascertain the sticking probability.

Findings show that the Lagrangian time scale T_L, in the range between 6 and 10 μs, does not influence the clogging significantly for the current benchmark. If the value of T_L is excessive, this is not desirable, because it may cause a particle to cross the computational cell in one step. If T_L is too small, particles would hardly come into contact with the wall, due to the state of particle motion (sweep, diffusion, or ejection) changes too frequently. As shown in Fig. 16, the case with $T_L = 2$ μs has a lower deposition rate than the case with $T_L = 6$ and 10 μs. To the authors' knowledge, there is no reliable criterion to identify T_L under different conditions.

According to Fig. 18(b), when a larger value is applied for the correction power (n) in the interpolation of clog permeability, Eq. (22), the bulge-branch transition of the clog occurs sooner. The larger the n value, the more permeable the partially clogged cells become. When a particle enters one of these cells, it can leave this cell into its neighboring partially clogged cells with greater ease; the bulge-branch transition occurs sooner. An excessive n value leads to an unphysical overestimation of permeability. Additionally, if n is too large, this introduces a convergence problem, because it makes the curve of $1/K_{per}$ (Fig. 18(a)), or Darcy source term, as a stepwise function. With $n = 1$, i.e. linear interpolation, the permeability of a cell decreases extraordinarily, resulting in a tiny amount of particle deposition, which is not reasonable.

The model can treat the clog as a porous medium, either with large open pores or with randomly packed spheres (Fig. 19). This is determinable by the post-mortem analysis of the clog structure. In actual fact, the clog structure is the outcome of the particle-particle and particle-fluid interactions. These interactions differ for different fluids and particles. Therefore, to perform a reliable simulation, it is crucial to have a sound knowledge of clog structures. Currently, the correlation of clog structures with the inclusion types and steel grades is not well-established. Therefore, the present model is limited to experimental data analysis after clogging for certain conditions. Further numerical and experimental studies will be required to obtain correlations of the clog structure with the NMIs and melt.

NMIs in steel melt are not only spherical, they are often found in the form of clusters, column, or faceted particles [26–30]. The shape of the particle influences the clogging behavior. For example, in the laboratory experiments, when major inclusions are in the form of large clusters, the nozzle is found to be blocked by clogging in the upper section [12,55]. This, hence, means that new features should be implemented in the model to deal with different shapes of particles. Another point of concern is the probable solidification near the SEN wall during continuous casting of steel. It can affect the behavior of the particles near the wall and the strength of the clog against the melt flow [21,22]. A further point is the sticking probability of the particle when it hits the nozzle wall. A sticking probability of 100% is here assumed according to the evidence as found in the literature [48–50], but it is also believed that the sticking probability might depend on the wall roughness, local temperature, and the wettability of wall and particles by the melt [6].

The current model is based on many model assumptions. Some of them are necessary, because a precise description of some physical or chemical processes is not available, while some assumptions can be improved in future, i.e. more physical or more chemical processes will be included in the model. They are discussed as follows:

- Transport of particle in the bulk melt and in the near-wall region has to be considered differently. The border between bulk and near-wall regions is defined by $y^+ = 100$ according to the boundary layer theory. However, we apply the near-wall model only for wall-bounded cells due to the difficulty in the calculation of y^+ in the interior cells during clog growth. However, the calculation might not ideally fulfill the condition for the whole thickness of the boundary layer. As a wall-bounded cell is >50% occupied by the clog layer, it is numerically treated as a cell of porous medium. The flow might not behave in coherent structures in the neighboring cell (or cells) anymore. Then there is no wall boundary; instead, there is only clog front with porous medium.
- Currently, when a particle reaches the wall or clog front, there is no chance of it returning to the bulk fluid, i.e. the 'sticking probability' is set 100%. This assumption seems reasonable according to some observations [47]. However, we still believe that this sticking probability could depend on following chemical or physical processes: chemical reactions on the SEN wall or on the NMI surface which alter their wettability, presence of gas bubble or liquid film of other phases near the wall [51], and energy barrier or repulsive forces when the particle is approaching the wall, etc.; further study is needed.
- There is ongoing debate concerning the solidification of steel on the SEN wall as one of the clogging mechanisms. Some experiments appear to counter this idea [29,53] because it has been proven that clogging still occurs in the continuously-heated nozzle as the isothermal steel melt transverses it. Some industrial practices lead to relatively large amounts of steel occasionally being found in the clog layer from the post-mortem analysis of the clog sample [21]. More experimental investigations and modeling efforts are required to establish how significantly the temperature gradient and solidification will affect clogging behavior in SEN. Hence, the thermal field and solidification should be considered in the future models.

Parameters for describing the clog morphology, d_p, $\overline{f}_p$ and D_{pore}, are assumed as constants. Average values are estimated, based on the post-mortem analysis of the clog sample. Conducting a study on the variation/distribution of above parameters would be beyond the scope of this paper, but the how sensitively the values correlate with the modeling result could be the subject of investigations.

6. Conclusions

A transient model considering two-way coupling between clog growth (due to particle deposition) and fluid flow is proposed for simulating the clogging phenomenon in a submerged entry nozzle (SEN) during continuous casting of steel. The model has considered critical steps of the clogging: transport of particles by turbulent flow towards the wall; wall-fluid interactions and adhesion mechanism of deposition; formation and growth of the clog due to particle deposition. The model is validated by reproducing a laboratory experiment, which was designed to study clogging in SEN.

(1) The numerically-calculated clogged section of the nozzle is qualitatively comparable with typically as-clogged sections in laboratory experiments.
(2) The calculated mass flow rate through the nozzle during the clogging process as a function of time also agrees with the experimentally-monitored result.

New knowledge about clogging can be derived from the modeling results.

(1) Clogging is a transient process, and it includes the initial coverage of the nozzle wall with deposited particles, the evolution of a bulged clog front, and then the development of a branched structure.
(2) Clogging is a stochastic and self-accelerating process.

Uncertainties for modeling parameters such as mesh size, Lagrangian time scale (T_L), correction factor (n) in the interpolation of clog permeability, and porosity in the clog materials, are being studied.

(1) The modeling result on particle deposition becomes insensitive to T_L and n when they are set at close to 6 μs and 5, respectively.
(2) In order to estimate the permeability of the clog, the clog materials can be treated as a porous medium, either with large open pores or with randomly packed spheres.
(3) In order to achieve significant results from the early stage of clogging, using a very fine mesh is recommended for the wall boundary cells (≤0.1 mm in the studied case). Due to the stochastic nature of clog growth and the limitations of the computer hardware, it is not possible to resolve the clog front structure in details for the later stage of clogging in the inner nozzle region.

The current model is still subjected to further refinements. In order to simulate the clogging with quantitative accuracy, following points are needed to be included:

(1) particles with non-spherical shapes;
(2) probable solidification on the SEN wall;
(3) porosity and morphological structure of clog as a function of the size and shape of particles;
(4) more accurate physical or chemical mechanisms of particle sticking to the nozzle wall.

Nomenclature

Symbol	Unit	Meaning
C_μ	-	Turbulence constant
C_D	-	Drag coefficient
D_ω	kg/(m^2.s^2)	Cross-diffusion term of ω
D_{pore}	m	Pore diameter in clog
d_p	m	Diameter of particle
$\vec{F}_B$	kg.m/s^2	Buoyancy force
$\vec{F}_D$	kg.m/s^2	Drag force
$\vec{F}_L$	kg.m/s^2	Lift force
$\vec{F}_{press}$	kg.m/s^2	Pressure gradient force
$\vec{F}_{VM}$	kg.m/s^2	Virtual mass force
$\overline{f}_p$	-	Average volume fraction of solid particles
G	1/s	Local velocity gradients
f_{clog}	-	Volume fraction of clog
$\tilde{G}_k, G_\omega$	kg/(m.s^3), kg/(m^2.s^2)	Generation of turbulence kinetic energy for k and ω
$\vec{g}$	m/s^2	Gravity
J	-	Correction factor of the lift force
K	m/s$^{3/2}$	Diffusion coefficient
K_{Br}	m/s$^{3/2}$	Velocity diffusion term
K_{per}	m^2	Permeability
K_s	m	Physical roughness height
K_s^+	-	Non-dimensional roughness height
k	m^2/s^2	Turbulence kinetic energy
m_p	kg	Mass of particle
n	-	Interpolation correction power
p	Pa	Pressure of fluid
R_a	m	Arithmetic average of distances from the average height
Re_P	-	Particle Reynolds number

S	-	Parent process for stochastic model
$S_k, S_\omega, \vec{S}_u$	kg/(m.s^3), kg/(m^2.s^2), kg/(m^2.s^2)	Source term due to porous medium of clog
T_L	s	Lagrangian time scale
Th_{clog}	m	Thickness of clog
t	s	Time
U_s	m/s	Difference between instantaneous streamwise velocities for fluid and particle
$\overline{u}$	m/s	Time averaged velocity of fluid
$\overrightarrow{u}$	m/s	Instantaneous velocity of fluid
$\overrightarrow{u}_p$	m/s	Velocity of particle
u_s	m/s	Wall normal velocity of the fluid seen by the particle
u^*	m/s	Velocity function
ΔV	m^3	Volume of cell
W	-	Wiener process
Y_k, Y_ω	kg/(m.s^3), kg/(m^2.s^2)	Dissipation of k and ω
Γ_k, Γ_ω	kg/(m.s), kg/m^2	Diffusivity for k and ω
μ	kg/(m.s)	Viscosity of fluid
ξ	-	Gaussian distributed random number
ρ	kg/m^3	Density of fluid
ρ_p	kg/m^3	Density of particle
τ_p	s	Particle relaxation time
ω	1/s	Specific dissipation rate of turbulence kinetic energy

Acknowledgments

The research leading to these results has received funding from the European Union's Research Fund for Coal and Steel (RFCS) research program under grant agreement No RFSR-CT-2014-00009. The authors also gratefully acknowledge the funding support of K1-MET, metallurgical competence center. The research program of the K1-MET competence center is supported by COMET (Competence Center for Excellent Technologies), the Austrian program for competence centers. COMET is funded by the Federal Ministry for Transport, Innovation and Technology, the Federal Ministry for Science, Research and Economy, the provinces of Upper Austria, Tyrol and Styria as well as the Styrian Business Promotion Agency (SFG).

References

[1] T. Schwarz, Heat transfer and fouling behaviour of Siemens PWR steam generators–long-term operating experience, Exp. Thermal Fluid Sci. 25 (2001) 319–327, https://doi.org/10.1016/S0894-1777(01)00080-2.
[2] M.S. Abd-Elhady, M.R. Malayeri, H. Müller-Steinhagen, Fouling problems in exhaust gas recirculation coolers in the automotive industry, Heat Transfer Eng. 32 (2011) 248–257, https://doi.org/10.1080/01457632.2010.495612.
[3] A. Vernhet, D. Cartalade, M. Moutounet, Contribution to the understanding of fouling build-up during microfiltration of wines, J. Membr. Sci. 211 (2003) 357–370, https://doi.org/10.1016/S0376-7388(02)00432-5.
[4] L.D. Nghiem, S. Hawkes, Effects of membrane fouling on the nanofiltration of pharmaceutically active compounds (PhACs): mechanisms and role of membrane pore size, Sep. Purif. Technol. 57 (2007) 176–184, https://doi.org/10.1016/j.seppur.2007.04.002.
[5] B.G. Thomas, H. Bai, Tundish nozzle clogging-application of computational models, Steelmak. Conf. Proc 2001, pp. 895–912.
[6] C. Henry, J.-P.P. Minier, G. Lefèvre, Towards a description of particulate fouling: from single particle deposition to clogging, Adv. Colloid Interf. Sci. 185–186 (2012) 34–76, https://doi.org/10.1016/j.cis.2012.10.001.
[7] P. Adomeit, U. Renz, Deposition of fine particles from a turbulent liquid flow: experiments and numerical predictions, Chem. Eng. Sci. 51 (1996) 3491–3503, https://doi.org/10.1016/0009-2509(95)00402-5.
[8] F. Kuhnen, K. Barmettler, S. Bhattacharjee, M. Elimelech, R. Kretzschmar, Transport of iron oxide colloids in packed quartz sand media: monolayer and multilayer deposition, J. Colloid Interface Sci. 231 (2000) 32–41, https://doi.org/10.1006/jcis.2000.7097.
[9] P. Bacchin, A. Marty, P. Duru, M. Meireles, P. Aimar, Colloidal surface interactions and membrane fouling: investigations at pore scale, Adv. Colloid Interf. Sci. 164 (2011) 2–11, https://doi.org/10.1016/j.cis.2010.10.005.
[10] L. Zhang, Y. Wang, X. Zuo, Flow transport and inclusion motion in steel continuous-casting mold under submerged entry nozzle clogging condition, Metall. Mater. Trans. B Process Metall. Mater. Process. Sci. 39 (2008) 534–550, https://doi.org/10.1007/s11663-008-9154-6.
[11] Y. Vermeulen, B. Coletti, B. Blanpain, P. Wollants, J. Vleugels, Material evaluation to prevent nozzle clogging during continuous casting of Al killed steels, ISIJ Int. 42 (2002) 1234–1240, https://doi.org/10.2355/isijinternational.42.1234.
[12] N. Kojola, S. Ekerot, P. Jönsson, Pilot plant study of clogging rates in low carbon and stainless steel grades, Ironmak. Steelmak. 38 (2011) 81–89, https://doi.org/10.1179/030192310X12706364542704.
[13] F.M. Najjar, B.G. Thomas, D.E. Hershey, Numerical study of steady turbulent flow through bifurcated nozzles in continuous casting, Metall. Mater. Trans. B Process Metall. Mater. Process. Sci. 26 (1995) 749–765, https://doi.org/10.1007/BF02651721.
[14] Y. Miki, H. Kitaoka, T. Sakuraya, T. Fujii, Mechanism for separating inclusions from molten steel stirred with a rotating magnetic field, ISIJ Int. vol. 32 (1992) 142–149, https://doi.org/10.2355/isijinternational.32.142.
[15] L. Zhang, B.G. Thomas, State of the art in the control of inclusions during steel ingot casting, Metall. Mater. Trans. B Process Metall. Mater. Process. Sci. 37 (2006) 733–761, https://doi.org/10.1007/s11663-006-0057-0.
[16] S. Basu, S.K. Choudhary, N.U. Girase, Nozzle clogging behaviour of Ti-bearing Al-killed ultra low carbon steel, ISIJ Int. 44 (2004) 1653–1660, https://doi.org/10.2355/isijinternational.44.1653.
[17] K. Sasai, Y. Mizukami, Reaction mechanism between alumina graphite immersion nozzle and low carbon steel, ISIJ Int. 34 (1994) 802–809, https://doi.org/10.2355/isijinternational.35.26.
[18] P.M. Benson, Q.K. Robinson, C. Dumazeau, New technique for the prevention of alumina build-up in submerged entry nozzles for continuous casting, Unitecr'93 Congr. Refract. New World Econ. Proc. Conf. Sao Paulo, 1993.
[19] G.C. Duderstadt, R.K. Iyengar, J.M. Matesa, Tundish nozzle blockage in continuous casting, JOM 20 (1968) 89–94.
[20] J.W. Farrell, D.C. Hilty, Steel flow through nozzles: influence of deoxidizers, Electr. Furn. Proc 1971, pp. 31–46.
[21] S. Rödl, H. Schuster, S. Ekerot, G. Xia, N. Veneri, F. Ferro, S. Baragiola, P. Rossi, S. Fera, V. Colla, et al., New Strategies for Clogging Prevention for Improved Productivity and Steel Quality, 2008.
[22] K.G. Rackers, B.G. Thomas, Clogging in continuous casting nozzles, 78th Steelmak. Conf. Proc 1995, pp. 723–734.
[23] R. Sambasivam, Clogging resistant submerged entry nozzle design through mathematical modelling, Ironmak. Steelmak. 33 (2006) 439–453, https://doi.org/10.1179/174328106X118198.
[24] M. Long, X. Zuo, L. Zhang, D. Chen, Kinetic modeling on nozzle clogging during steel billet continuous casting, ISIJ Int. 50 (2010) 712–720, https://doi.org/10.2355/isijinternational.50.712.
[25] L.F. Zhang, B.G. Thomas, State of the art in evaluation and control of steel cleanliness, ISIJ Int. 43 (2003) 271–291, https://doi.org/10.2355/isijinternational.43.271.
[26] L. Zhang, W. Pluschkell, Nucleation and growth kinetics of inclusions during liquid steel deoxidation, Ironmak. Steelmak. 30 (2003) 106–110, https://doi.org/10.1179/030192303225001766.
[27] R. Dekkers, B. Blanpain, P. Wollants, F. Haers, B. Gommers, C. Vercruyssen, A morphological comparison between inclusions in aluminium killed steels and deposits in submerged entry nozzle, Steel Res. Int. 74 (2003) 351–355.
[28] B.G. Thomas, Q. Yuan, S. Mahmood, R. Liu, R. Chaudhary, Transport and entrapment of particles in steel continuous casting, Metall. Mater. Trans. B Process Metall. Mater. Process. Sci. 45 (2014) 22–35, https://doi.org/10.1007/s11663-013-9916-7.
[29] D. Janis, A. Karasev, R. Inoue, P.G. Jönsson, A study of cluster characteristics in liquid stainless steel and in a clogged nozzle, Steel Res. Int. 86 (2015) 1271–1278, https://doi.org/10.1002/srin.201400316.
[30] Z. Deng, M. Zhu, Y. Zhou, D. Sichen, Attachment of alumina on the wall of submerged entry nozzle during continuous casting of al-killed steel, Metall. Mater. Trans. B Process Metall. Mater. Process. Sci. 47 (2016) 2015–2025, https://doi.org/10.1007/s11663-016-0624-y.
[31] S.N. Singh, Mechanism of alumina buildup in tundish nozzles during continuous casting of aluminum-killed steels, Metall. Trans. A. 5 (1974) 2165–2178.
[32] L. Trueba, K.D. Peaslee, J.D. Smith, M. Karakus, Effect of Nozzle Base material on the rate of clogging during the continuous casting of aluminum-killed steels, Steel Res. Int. 77 (2006) 37–47, https://doi.org/10.1002/srin.200606128.
[33] H. Bai, B.G. Thomas, Effects of clogging, argon injection, and continuous casting conditions on flow and air aspiration in submerged entry nozzles, Metall. Mater. Trans. B Process Metall. Mater. Process. Sci. 32 (2001) 707–722, https://doi.org/10.1007/s11663-001-0125-4.
[34] C. Pfeiler, B.G. Thomas, M. Wu, A. Ludwig, A. Kharicha, Solidification and particle entrapment during continuous casting of steel, Steel Res. Int. 79 (2008) 599–607, https://doi.org/10.1002/srin.200806172.
[35] Q. Yuan, B.G. Thomas, S.P. Vanka, Study of transient flow and particle transport in continuous steel caster molds: part II. Particle transport, Metall. Mater. Trans. B Process Metall. Mater. Process. Sci. 35 (2004) 703–714, https://doi.org/10.1007/s11663-004-0010-z.
[36] M. Mohammadi-Ghaleni, M. Asle Zaeem, J.D. Smith, R. O'Malley, Comparison of CFD simulations with experimental measurements of nozzle clogging in continuous casting of steels, Metall. Mater. Trans. B Process Metall. Mater. Process. Sci. 47 (2016) 1–10, https://doi.org/10.1007/s11663-016-0798-3.
[37] P. Ni, L.T.I. Jonsson, M. Ersson, P.G. Jönsson, The use of an enhanced Eulerian deposition model to investigate nozzle clogging during continuous casting of steel, Metall. Mater. Trans. B Process Metall. Mater. Process. Sci. 45 (2014) 2414–2424, https://doi.org/10.1007/s11663-014-0145-5.
[38] P. Ni, L.T.I. Jonsson, M. Ersson, P.G. Jönsson, On the deposition of particles in liquid metals onto vertical ceramic walls, Int. J. Multiphase Flow 62 (2014) 152–160, https://doi.org/10.1016/j.ijmultiphaseflow.2014.02.002.
[39] D. Eskin, J. Ratulowski, K. Akbarzadeh, Modeling of particle deposition in a vertical turbulent pipe flow at a reduced probability of particle sticking to the wall, Chem. Eng. Sci. 66 (2011) 4561–4572, https://doi.org/10.1016/j.ces.2011.06.015.

[40] C. Caruyer, J.-P. Minier, M. Guingo, C. Henry, A stochastic model for particle deposition in turbulent flows and clogging effects, in: P. Gourbesville, J.A. Cunge, G. Caignaert (Eds.), Adv. Hydroinformatics SIMHYDRO 2014, Springer Singapore, Singapore 2016, pp. 597–612, https://doi.org/10.1007/978-981-287-615-7_40.
[41] M. Wu, A. Ludwig, A three-phase model for mixed columnar-equiaxed solidification, Metall. Mater. Trans. A. 37 (2006) 1613–1631, https://doi.org/10.1007/s11661-006-0104-0.
[42] M. Wu, A. Ludwig, Using a three-phase deterministic model for the columnar-to-Equiaxed transition, Metall. Mater. Trans. A. 38 (2007) 1465–1475, https://doi.org/10.1007/s11661-007-9175-9.
[43] A. Fluent, Ansys fluent, Acad. Res. Release 14 (2015).
[44] A. Soldati, C. Marchioli, Physics and modelling of turbulent particle deposition and entrainment: review of a systematic study, Int. J. Multiphase Flow 35 (2009) 827–839, https://doi.org/10.1016/j.ijmultiphaseflow.2009.02.016.
[45] M. Guingo, J.-P. Minier, A stochastic model of coherent structures for particle deposition in turbulent flows, Phys. Fluids 20 (2008), 53303. https://doi.org/10.1063/1.2908934.
[46] J.-P. Minier, E. Peirano, The pdf approach to turbulent polydispersed two-phase flows, Phys. Rep. 352 (2001) 1–214, https://doi.org/10.1016/S0370-1573(01)00011-4.
[47] K. Uemura, M. Takahashi, S. Koyama, M. Nitta, Filtration Mechamism of non-metallic inclusions in steel by ceramic loop filter, ISIJ Int. 32 (1992) 150–156, https://doi.org/10.2355/isijinternational.32.150.
[48] F. Heuzeroth, J. Fritzsche, E. Werzner, M.A.A. Mendes, S. Ray, D. Trimis, U.A. Peuker, Viscous force - an important parameter for the modeling of deep bed filtration in liquid media, Powder Technol. 283 (2015) 190–198, https://doi.org/10.1016/j.powtec.2015.05.018.
[49] E. Kawecka-Cebula, Z. Kalicka, J. Wypartowicz, Filtration of nonmetallic inclusions in steel, Arch. Metall. Mater. 51 (2006) 261–268.
[50] K. Sasai, Y. Mizukami, Mechanism of alumina adhesion to continuous caster nozzle with Reoxidation of molten steel, ISIJ Int. 41 (2001) 1331–1339, https://doi.org/10.2355/isijinternational.41.1331.
[51] M. Thumfart, M. Javurek, Low pressure effects in SEN-stopper region in continuous casting, Steel Res. Int. 86 (2015) 25–32, https://doi.org/10.1002/srin.201300448.
[52] T. Adams, C. Grant, H. Watson, A. Simple Algorithm, To relate measured surface roughness to equivalent sand-grain roughness, Int. J. Mech. Eng. Mechatron. 1 (2012) 66–71, https://doi.org/10.11159/ijmem.2012.008.
[53] E. Roos, A. Karasev, P.G. Jönsson, Effect of Si and Ce contents on the nozzle clogging in a REM alloyed stainless steel, Steel Res. Int. 86 (2015) 1279–1288, https://doi.org/10.1002/srin.201400344.
[54] X. Yang, T.J. Lu, T. Kim, An analytical model for permeability of isotropic porous media, Phys. Lett. A 378 (2014) 2308–2311, https://doi.org/10.1016/j.physleta.2014.06.002.
[55] N. Kojola, S. Ekerot, M. Andersson, P.G. Jönsson, Pilot plant study of nozzle clogging mechanisms during casting of REM treated stainless steels, Ironmak. Steelmak. 38 (2011) 1–11, https://doi.org/10.1179/030192310X12690127076398.
[56] P. Ni, L. Jonsson, M. Ersson, P.G. Jönsson, Turbulent flow phenomena and Ce2O3 behavior during a steel teeming process, ISIJ Int. 53 (2013) 792–801, https://doi.org/10.2355/isijinternational.53.792.
[57] K. Sasai, Y. Mizukami, Effect of stirring on oxidation rate of molten steel, ISIJ Int. 36 (1996) 388–394, https://doi.org/10.2355/isijinternational.36.388.
[58] F.R. Menter, Two-equation eddy-viscosity turbulence models for engineering applications, AIAA J. 32 (1994) 1598–1605, https://doi.org/10.2514/3.12149.
[59] F.R. Menter, M. Kuntz, R. Langtry, Ten years of industrial experience with the SST turbulence model, Turbul. Heat Mass Transf. 4 (2003) 625–632.
[60] C. Henry, J.P. Minier, Progress in particle resuspension from rough surfaces by turbulent flows, Prog. Energy Combust. Sci. 45 (2014) 1–53, https://doi.org/10.1016/j.pecs.2014.06.001.
[61] A. Jungreithmeier, E. Pissenberger, K. Burgstaller, J. Mortl, Production of ULC IF steel grades at Voestalpine Stahl GmbH, Linz, Iron Steel Soc. Int. Technol. Conf. Expo. 2003 2003, pp. 227–240.